Study of the Reaction $\bar{p}\,p \to \overline{\Lambda}\,\Lambda$ at 1.546 and 1.695 GeV/c

P.D. Barnes, G. Diebold, G. Franklin, C. Maher, B. Quinn and J. Seydoux
Carnegie-Mellon University, Pittsburgh, PA 15213, USA

K. Kilian[1]
CERN, CH-1211 Geneva 23, Switzerland

R. Besold, W. Eyrich, R.v. Frankenberg, A. Hofmann[†], D. Malz, F. Stinzing and P. Woldt
University of Erlangen-Nürnberg, D-8520 Erlangen, Fed. Rep. Germany

P. Birien, W. Dutty, J. Franz, N. Hamann[2], E. Rössle, H. Schledermann
H. Schmitt and H.-J. Urban
University of Freiburg, D-7800 Freiburg, Fed. Rep. Germany

R.A. Eisenstein and D. Hertzog
University of Illinois, Urbana-Champaign, IL 61820, USA

W. Oelert and G. Sehl
Institut für Kernphysik der KFA, D-5170 Jülich, Fed. Rep. Germany

B.E. Bonner[3]
Los Alamos National Laboratory, Los Alamos, NM 87545, USA

G. Ericsson[4], T. Johansson and S. Ohlsson
Uppsala University, S-75121 Uppsala, Sweden

W.H. Breunlich and P. Pawlek
Institut für Mittelenergiephysik der ÖAW, A-1090 Vienna, Austria

Abstract: The PS185 experiment at the CERN Low Energy Antiproton Ring (LEAR) has studied the reaction $\bar{p}p \to \overline{\Lambda}\Lambda$ at several momenta. In this paper results from two runs with high statistics at 1.546 GeV/c and 1.695 GeV/c are described. Based on 4063 and 11362 analysed events, respectively, differential and integrated cross sections, polarizations and spin correlations are presented. The singlet fraction, extracted from the spin correlations, is consistent with zero at both momenta, showing that the $\overline{\Lambda}\Lambda$ pairs are produced in a pure triplet state. A comparison of the decay asymmetry parameters of Λ and $\overline{\Lambda}$ reduces the upper limits for the violation of the CP invariance for this system.

> E REACTION: $\bar{p}p \to \overline{\Lambda}\Lambda$; $p_{\mathrm{Lab}} = 1.546, 1.695\,\mathrm{GeV}/c$; measured σ, $\sigma(\theta)$, polarization, and spin correlation.

(Submitted to Nuclear Physics A)

† deceased.

Present addresses:
1) Institut für Kernphysik der KFA, D-5170 Jülich, Fed. Rep. Germany.
2) CERN, CH-1211 Geneva 23, Switzerland.
3) Rice University, Houston, TX 77251, USA.
4) Lund University, S-22362 Lund, Sweden.

1 Introduction

The exclusive production of hyperon–antihyperon pairs in the reactions $\bar{p}p \to \bar{\Lambda}\Lambda$, $\bar{p}p \to \bar{\Lambda}\Sigma$ and $\bar{p}p \to \bar{\Sigma}\Sigma$ represents a small fraction (10^{-3} to 10^{-4}) of the total $\bar{p}p$ cross section. The associated production of strangeness in these reactions, however, offers the opportunity of studying aspects of the interaction and, in particular, the spin dynamics of the produced strange–antistrange quark pair.

The lowest order quark–line diagram for the reaction $\bar{p}p \to \bar{\Lambda}\Lambda$ is shown in Fig. 1a. In the static quark model [1-3] this reaction is described by the annihilation and creation of an 'active' quark–antiquark pair, while the other quarks act as 'spectators'. These spectator quarks form spin- and isospin-singlet diquarks (ud and $\bar{u}\bar{d}$), and therefore in this model the polarization measured for the (anti–)hyperon is identical to the polarization of the ($\bar{s}$)s quark. The spin correlations are thus directly related to the spin state of the $\bar{s}s$ pair. The simple assumption, that the polarization of the Λ hyperon is carried by the s quark, is supported by a study of the reaction $\bar{p}Be \to \Lambda X$ using a polarized proton beam at BNL. The measured Λ polarization appears to be independent of the incident proton polarization [4].

The quantum numbers of the $\bar{s}s$ vertex can be derived in the framework of the static quark model from a measurement of the reaction $\bar{p}p \to \bar{\Lambda}\Lambda$ near its kinematical threshold ($p_{\text{thrsh}} = 1.435 \, \text{GeV}/c$), where only a few partial waves contribute to the production process [5]. If the $\bar{\Lambda}\Lambda$ are produced in a relative S–state and the final–state is a spin triplet, the $\bar{s}s$ vertex has 'gluon quantum numbers', $J^P = 1^-$. In the case of pure P–wave production and final state spin triplet, the vertex has 'vacuum quantum numbers', $J^P = 0^+$.

It is well known experimentally that hyperons, produced at higher energies in reactions like $\bar{p}p \to \bar{\Lambda}\Lambda$ [6], $\bar{p}p \to \bar{\Sigma}\Lambda$ [6], $\pi^-p \to K^\circ\Lambda$ [7], $\gamma p \to K^+\Lambda$ [8] and $pA \to \Lambda X$ [9] exhibit large polarizations of the order of $|P| \approx 0.5$. The polarization increases with increasing transverse momentum (p_T) and saturates at $p_T \approx 1 \, \text{GeV}/c$. For a given reaction the polarization is nearly independent of the centre–of–mass energy.

The measurements of $\bar{p}p \to \bar{\Lambda}\Lambda$ at LEAR have stimulated several theoretical works [10-23]. The descriptions are of two general types. In the 'quark picture' one can assume that the $\bar{s}s$ pair creation is mediated by an s–channel 'pseudo gluon exchange'. Here an odd number of gluons exchanged would lead to the quantum numbers $J^P = 1^-$ at the vertex (the $^3S_1$ model), while an even number of exchanged gluons is represented by a 0^+ exchange (e.g. the $^3P_0$ model). In a more 'conventional' approach the reaction $\bar{p}p \to \bar{\Lambda}\Lambda$ is described by a t–channel meson–exchange picture (Fig. 1b), where a potential derived from kaon exchange is used for calculations. The strange–meson exchange corresponds to the quark line diagram where a $\bar{u}u$ quark–pair annihilation is followed by a $\bar{s}s$ creation in the direct channel (Fig. 1a). In the boson–exchange picture, as well in the quark–line picture, the initial– and final–state interactions have been shown to be of great importance.

The first measurements of the reaction $\bar{p}p \to \bar{\Lambda}\Lambda$ with experiment PS185 at the LEAR facility at CERN covered the momentum range from threshold at

2

1.435 GeV/c to 1.508 GeV/c [5,24]). In this paper we report on measurements of the reaction $\bar{p}p \to \bar{\Lambda}\Lambda$ at two higher beam momenta: 1.546 GeV/c and 1.695 GeV/c. These momenta correspond to excess energies above threshold ($\epsilon = \sqrt{s} - 2m_\Lambda$, where $\sqrt{s}$ is the invariant mass) of $\epsilon = 39.1$ MeV and $\epsilon = 91.7$ MeV, respectively. At these two energies 4063 and 11362 $\bar{\Lambda}\Lambda \to \bar{p}\pi^+p\pi^-$ events, respectively, have been analysed. Differential and integrated cross sections as well as polarizations and spin correlations are presented. The high statistics at 1.695 GeV/c allowed a reduction of the upper limit on the ratio $A = (\alpha + \bar{\alpha})/(\alpha - \bar{\alpha})$ of the asymmetry parameters $\bar{\alpha}$ and α for the weak $\bar{\Lambda}$ and Λ decays, for which a value of zero is required from CP invariance [25]).

2   Experiment

The design of the PS185 detector is matched to the production- and decay-kinematics for the antihyperon–hyperon pairs $\bar{\Lambda}\Lambda$, $\bar{\Lambda}\Sigma$ and $\bar{\Sigma}\Sigma$ emerging from $\bar{p}p$ interactions. In the momentum range accessible at LEAR ($p_{\bar{p}} \leq 2$ GeV/c) the production angle for hyperons in the laboratory system is limited to about 32°. The decay (anti–)baryons are emitted within narrow forward cones around the (anti–)hyperon directions, the maximum angle (with respect to the incident antiproton direction) being about 41°. The detector covers this angular range, and therefore has a 4π acceptance for the decay (anti–)baryons. The pions from the hyperon decays can be emitted at all angles, leading to an angle–dependent acceptance for the decay pions.

A plan view of the experimental set–up, with an overlay of an identified $\bar{\Lambda}\Lambda \to \bar{p}\pi^+p\pi^-$ event, is shown in Fig. 2. The detector consists of four basic elements: an active–trigger target system; sets of multiwire proportional chambers and drift chambers for charged–particle track reconstruction; a scintillator hodoscope for fast trigger purposes, and a solenoidal magnet with enclosed drift chambers for baryon–number identification.

2.1   Target System

With typical rates of 1×10^5 to 5×10^5 antiprotons per second, the beam was focussed to a spot size of 0.7×1.2 mm^2 (FWHM in the horizontal and the vertical direction, respectively) on a target system (Fig. 2). This target system is used to trigger on the incident antiproton and to veto prompt charged particles. The incoming beam is defined by two scintillation counters S1A·S1B, which are placed in front of the target system. The target consists of five equally structured cells (T1–T5), each of which contains a 2.5 mm long cylindrical slab with a diameter of 2.5 mm. The slabs in the last four cells (T2–T5) are made of polyethylene (CH$_2$) and serve as proton targets, whereas the first cell (T1) consists of pure carbon and is used to monitor the carbon background contribution. The cells are separated by 0.2 mm thick scintillation counters (S3), each of which serve as a veto for the preceding cell or as a beam tag for the following one. In addition, each target is surrounded by a 1.25 mm thick veto scintillation barrel (S2), which is used for suppressing background reactions involving charged particles. The trigger

for a 'neutral interaction' in a target cell is thus defined by $S1A \cdot S1B \cdot \overline{S2} \cdot \overline{S3}$, where S2 and S3 are the corresponding veto counters of that cell. The charged interaction rejection inefficiency was smaller than 10^{-5}. The advantages of the modular target structure are the increase of the target length without losing accuracy in the definition of the production vertex and without decreasing the trigger efficiency for neutral particles. For a measurement very close to threshold the modular target structure opens the possibility of a fine–step degradation of the incident antiproton momentum, corresponding to the mean momentum loss in each cell.

2.2   Track Recording

With a lifetime of 2.63×10^{-10} s, corresponding to a value of $c\tau = 7.89$ cm, the $\overline{\Lambda}$ and Λ hyperons, produced at $1.546\,(1.695)\,\mathrm{GeV}/c$ incident momentum, decay after a mean path of $3.7\,(3.1)$ cm to $7.3\,(8.8)$ cm depending on their momenta. The $\overline{\Lambda}\Lambda$ final state was identified by the measurement of the four tracks from the decay mode $\overline{\Lambda}\Lambda \rightarrow \overline{p}\pi^+ p\pi^-$, which has a branching ratio of $41.1\,\%$ [26]).

For the reconstruction of the decay V's (where 'V' means the charged–particle tracks from $\Lambda \rightarrow p\pi^-$ or $\overline{\Lambda} \rightarrow \overline{p}\pi^+$) a densely packed arrangement of 10 multiwire proportional chamber (MWPC) planes and 13 drift chamber (DC) planes was placed directly behind the target system (Fig. 2).

The wires of the MWPC planes are oriented alternately at $\pm 45°$ with respect to the horizontal. Each of the MWPC planes contains 160 gold plated tungsten wires with a diameter of $20\,\mu$m spaced 1.27 mm apart, and it spans an active area of 20.3×20.3 cm^2. The wire planes are spaced 1 cm apart and are separated by a cathode plane made of an aluminum foil of $10\,\mu$m thickness.

The drift chamber wires are oriented horizontally (x) and vertically (y). Each plane contains 14 drift cells of 4 cm width and spans an active area of 56×61 cm^2. They are read out by a pair of sense wires separated by 0.4 mm to resolve the left–right ambiguity. Each of the cathode planes contains $80\,\mu$m wires, spaced 2 mm apart. A graded potential, applied to the cathode wires, creates an approximately uniform drift field and thus ensures a nearly constant drift velocity. The efficiencies of the DC–planes vary between 89 and 96 % with an average efficiency of 92 %.

A difficulty in the use of wire doublets is the electrostatic repulsion of adjacent wires, which creates a sagitta $\Delta y \propto L^2/y$ of the wires, where L is the length and y is the spacing of the wires. This would lead to an intolerable distortion of $\Delta y = 1.5$ mm. Therefore the sense wires are often mechanically linked together with droplets of epoxy glue [27]. In our case, however, this would lead to a substantial decrease of the overall efficiency and another technique was developed [28]: A $10\,\mu$m nylon fibre is welded to the sense wire pairs every 12 to 15 cm along the wire doublets, which reduces the sagitta to $\Delta y = 60$ to 90 μm under normal operation. When integrated over the whole chamber plane, the efficiency loss due to these links is less than $0.1\,\%$.

The primary beam passes through the centre of all chamber planes. Therefore the central regions in these chambers had to be desensitized. This was done by

4

increasing the diameter of the central wire from 20 to $80\,\mu m$ over a length of 3 mm (in the first MWPC plane) to 12 mm (in the last DC plane) by electroplating a layer of silver onto it. Thus the electrical field does not reach the critical value for gas amplification, and the detection of particles in the desensitized regions is suppressed to the level 2×10^{-3} [28]).

2.3 Trigger Hodoscope

Behind the chamber stack a scintillation hodoscope is positioned. It consists of two sets of 20 elements, each having a size of $62 \times 3\,cm^2$ and a thickness of 4 mm, oriented in the $x-$ and $y-$directions. Four additional elements, $30.5 \times 1\,cm^2$ in size, are mounted in the centre of the hodoscope, leaving an opening of $1\,cm^2$ for the primary beam. The signals are read out with photomultiplier tubes at both ends of the elements (for the central elements only at the outer end). A signal from each hodoscope plane together with the 'neutral interaction trigger' from the target completes a full 'charged–neutral–charged' event trigger. In order to optimize the geometry for each incident momentum, corresponding to a certain maximum angle of the decay baryons, the target system and the chamber stack are mounted on rails and can be moved with respect to the hodoscope and the magnetic baryon–number identifier.

2.4 Baryon–Number Identifier

The $\overline{\Lambda}$ and Λ hyperons cannot be distinguished by the reconstruction of their decays. Therefore, a magnetic solenoid with its field in the vertical direction was placed downstream of the hodoscope. From the deflection of tracks, which is measured by three drift chambers inside the solenoid, the charge sign of the decay particles can be determined. The drift chambers are of the same basic cell geometry as described before. They have active areas of $64 \times 70\,cm^2$, $92 \times 94\,cm^2$, and $116 \times 116\,cm^2$, and give horizontal–position information. This arrangement has 100 % geometrical acceptance for both decay baryons from $\overline{\Lambda}\Lambda \rightarrow \overline{p}\pi^+p\pi^-$ at $1.546\,GeV/c$ and for at least one of the decay baryons at $1.695\,GeV/c$. The magnetic field is produced by water–cooled aluminium coils of trapezoidal shape. A 5 cm gap between two of the coil segments and a hole of 5 cm diameter in the rear flux–return yoke of the solenoid allow the passage of the primary beam. With a current of 1200 A a magnetic field of 0.1 T is obtained. The inhomogeneities of this field are less than 8 %. Outside the solenoid, in the region of the wire chamber stack, the field is smaller than 0.005 T and thus does not have a measurable influence on the charged–particle tracks or on the hyperon spin vectors.

3 Data Analysis

3.1 Event Selection

The analysis is based on events with two V's from the decays $\overline{\Lambda}\Lambda \rightarrow \overline{p}\pi^+p\pi^-$. The event selection proceeds in the following basic steps: Two–dimensional tracks are fitted to chamber hits in the four projections measured by the MWPC and

the DC planes. The typical single–wire spatial resolutions, determined from the standard deviations of line fits to small–angle tracks, are $\sigma = 0.34\,\mathrm{mm}$ in the MWPC and $\sigma = 0.15\,\mathrm{mm}$ in the DC. After a matching of two–dimensional to three–dimensional tracks a search for V's is started. The number of false V's is reduced by applying geometrical cuts, based on the coplanarity requirement for the decay planes and on the polar–angle correlation for the vertex points. With the remaining V's a full kinematical fit with 14 independent parameters is performed under the hypothesis of the event type $\overline{p}p \rightarrow \overline{\Lambda}\Lambda \rightarrow \overline{p}\pi^+ p\pi^-$.

The starting values for the kinematical fit are obtained by two alternative and complementary methods. In the first case the intersection of the two measured decay planes for $\overline{\Lambda}$ and Λ are determined to give the orientation of the antihyperon–hyperon production plane. The decay planes themselves intersect the production plane along the directions of the hyperons. From the corresponding angles the required centre–of–mass angles for the kinematical fit can be determined. This method does not depend on the knowledge of the production and decay–vertex points and therefore works well, in particular for short decay lengths.

The second method uses the production and decay points to determine the angles of the hyperons in the laboratory and therefore also in the centre–of–mass system. The second method is applied if the first one shows problems. This happens more often for longer decay paths, because the decay planes are less well determined in that case, and in the vicinity of the maximum hyperon production angle, where, owing to experimental uncertainties, kinematically impossible solutions become more likely. In both methods the baryon and pion of each decay vertex can be distinguished by their different angles with respect to the hyperon direction because of transverse–momentum conservation.

The reduced χ^2–distributions of the kinematical fit are shown in Fig. 3 at both incident momenta. A $\overline{\Lambda}\Lambda$ event is defined somewhat arbitrarily as one having reduced $\chi^2 < 5$.

3.2   Baryon–Number Identification

For the identification of the V's it is sufficient to measure the sign of the charge of only one decay particle, since the pion and the baryon are already separated by the kinematical fit. The coordinates measured by the three DC's inside the solenoid are used to calculate the sagitta of each track. We define the sagitta as the displacement of a charged–particle track at the position of the middle drift chamber with respect to a straight line, which is determined by the coordinates of the outer drift chambers within the solenoid. By this definition the sagitta is independent of the multiple scattering in the aluminum coils. With the magnetic field in the y–direction (Fig. 2), negatively charged particles are deflected to the right with respect to the particle direction, corresponding to a positive sign of the sagitta. From the momenta and directions of the particles, determined by the kinematical fit, and the known magnetic field, the expected sagittas can be calculated for both left– and right–bending. Using the experimentally determined sagitta values and their errors, a χ^2–test was performed in order to find the correct

6

assignment of the sign charge for each track. Only events with a reduced $\chi^2 \leq 9$ were accepted as 'identified'. If the sagittas of more than one track were measured, the upper identification criterion was based on the average reduced χ^2 of those tracks.

The separation between antiparticles and particles is illustrated in Fig. 4 where the sagitta distributions of the decay baryons and pions for a magnetic field of 0.1 T are displayed at both incident momenta. The different shapes and contents of the distributions for $\bar{p}$ and p, and for π^- and π^+ are explained by the differential cross sections (subsection 4.1), which show that the $\bar{\Lambda}$ is preferentially emitted at smaller forward angles. Therefore the $\bar{\Lambda}$ and its decay particles $\bar{p}$ and π^+ have on an average higher momenta, leading to smaller absolute values of the sagitta as compared with $\Lambda \rightarrow p\pi^-$. The lower Λ momenta correspond to larger laboratory angles for the decay particles p and π^-, leading to smaller contents in the sagitta distributions. The effect is more pronounced at the higher incident momentum 1.695 GeV/c for kinematical reasons and because of the smaller geometrical acceptance of the baryon–number identification at that momentum.

The efficiency of the baryon–number identification was determined by dividing the number of events with identified baryon–number by the number of kinematically identified $\bar{\Lambda}\Lambda$ events as a function of the absolute value of $\cos\theta_{\bar{\Lambda}}$, where $\theta_{\bar{\Lambda}}$ is the $\bar{\Lambda}$ centre–of–mass angle. The efficiency varies between 85 % and 93 % at both incident momenta. Its angular dependence was fitted by second order polynomials in order to correct the differential cross sections.

From the sagitta distributions of the baryons in Fig. 4 one can see that there exists a small number of events with a wrong baryon–number assignment, which is due to overlapping peaks. This affects the angular distribution in such a way that a fraction of events from the bin at $\cos\theta_{\bar{\Lambda}}$ is put into the bin at $-\cos\theta_{\bar{\Lambda}}$ and vice versa. The fraction of events with misidentified baryon–number was (2 ± 1) % at 1.546 GeV/c and (1.8 ± 0.3) % at 1.695 GeV/c. With these numbers the angular distributions were corrected according to

$$N_{\text{corr}}(x) = N(x) \cdot \left[\frac{1 - r\left(1 + \frac{N(-x)}{N(x)}\right)}{1 - 2r} \right] \qquad \text{with } x = \cos\theta_{\bar{\Lambda}}, \qquad (1)$$

where r is the fraction of misidentifications and $N(x)$ is the uncorrected number of events in the bin x. The polarizations and spin correlations can also be corrected for the baryon–number misidentification in a similar way [29]. The corrections in the case of the polarizations and spin correlations, however, turned out to be about one order of magnitude smaller than the statistical errors of these observables and could therefore be omitted.

3.3   Carbon Background

The background due to $\bar{\Lambda}\Lambda$ events produced on carbon via the reaction $\bar{p}C \rightarrow \bar{\Lambda}\Lambda + X$ was investigated by analyzing the data from the carbon target cell using the same algorithm and the same cuts as for the 'proton target' data. Events from the carbon cell with $\chi^2 < 5$ correspond to a contribution from the carbon in the four CH$_2$ targets of 9.8 % (8.6 %) in the data sample at 1.546 GeV/c

(1.695 GeV/c). This contribution is small, because a coplanarity cut and an angular cut on vertices is applied. The angular cut is set according to the maximum laboratory angle of the hyperons from $\bar{p}p \rightarrow \bar{\Lambda}\Lambda$, which is much smaller than the maximum angle of quasi–free $\bar{\Lambda}\Lambda$ production on carbon. The angular distributions for these events are shown in Fig. 5. It should be noted that this does not represent the differential cross sections for $\bar{\Lambda}\Lambda$ production on carbon, because the angular distributions contain only events that passed the cuts assuming the two–body reaction $\bar{p}p \rightarrow \bar{\Lambda}\Lambda$. For the subtraction from the angular distribution of the 'CH$_2$ target' events at 1.546 (1.695) GeV/c, the values are taken as obtained from fits to the distributions in Fig. 5 by Legendre polynomials up to the third (fourth) order.

The polarization and singlet fraction for events with $\chi^2 < 5$ from the carbon cell are shown in Fig. 6 at 1.695 GeV/c incident momentum. These results will be discussed in subsections 4.3 and 4.4.

3.4 Monte Carlo Study

A Monte Carlo program was used to generate the acceptance curve of the detector and the evaluation procedure. The detector performance was modelled by including effects such as the desensitized regions in the chambers, the chamber–plane resolutions and efficiencies, and the precise geometry of the veto counters surrounding the target cells. Simulated events were generated with an isotropic centre–of–mass angular distribution and without polarizations or spin correlations of the outgoing $\bar{\Lambda}\Lambda$ pairs. They were analysed in the same way as the actual data. The resulting acceptance curves are displayed in Fig. 7 and show a rather weak angular dependence at both incident momenta. The deviations from a 100 % acceptance are due to losses of the following three event types:

i) events with very short decay length, vetoed by the target counters (between 2 % and 5 % depending on the hyperon momenta);

ii) events with long decay length, outside the fiducial volume of reconstruction (between 9 % and 13 % depending on the hyperon momenta); and

iii) events with large–angle pion tracks ($\theta_\pi > 68°$ with respect to the z–axis), which cannot be reconstructed (between 25 % and 40 % depending on the hyperon momenta); these angles are more likely for low hyperon momenta, which occur preferentially at centre–of–mass angles in the vicinity of $|\cos\theta_{\bar{\Lambda}}| = 1$; this explains the decrease of the acceptance curves in this angular region.

3.5 Systematic Errors

The following systematic errors concern the absolute normalization of the cross sections:

i) Possible unrealistic assumptions in the Monte Carlo program lead to an error of the acceptance correction. This error was estimated to be 5 %, based on a comparison of the χ^2–distributions for measured and simulated events.

ii) Geometrical misalignments of the target cells and the production of δ-electrons in the targets themselves, which trigger the nearby veto counters, lead to a correction of the flux of the incoming antiprotons for each individual target cell. The uncertainty of this correction is 5 %, determined by a comparison of the numbers of $\overline{\Lambda}\Lambda$ events from each target cell obtained after the flux correction. These numbers are expected to be equal except for small devations due to the different cross section for each target cell, because of incident momentum degradation in each target.

iii) The double-branching ratio for $\overline{\Lambda}\Lambda \to \overline{p}\pi^+ p\pi^-$ has an uncertainty of 1.6 %.

iv) The corrections of the angular distributions for the efficiency of the baryon-number identification has an error of 1 % at both incident momenta.

The quadratic sum of these errors gives an uncertainty of the absolute normalization of the cross sections of 7.3 % at both incident momenta.

The following sources of systematic errors proved to be negligible:

Events of the two-vertex type, like $\overline{p}p \to K_S K_S X$, have different kinematics than $\overline{\Lambda}\Lambda$ production and thus do not have low χ^2 when fitted to the $\overline{p}p \to \overline{\Lambda}\Lambda$ hypothesis. The fraction of $K_S K_S X$ events with $\chi^2 < 5$ was found to be less than 0.1 %.

Losses of events due to the decay of pions or due to secondary interactions of the decay particles from $\overline{\Lambda}\Lambda \to \overline{p}\pi^+ p\pi^-$ on detector materials lead to a correction of the cross sections of 1.9 % with a negligible uncertainty of 0.3 %.

A systematic error could arise from events of the reaction $\overline{p}p \to \overline{\Lambda}\Sigma^o$ with the subsequent electromagnetic decay $\Sigma^o \to \Lambda\gamma$. This reaction has its kinematical threshold at 1.653 GeV/c beam momentum. The data taken at 1.695 GeV/c beam momentum have also been analysed looking for the reaction $\overline{p}p \to \overline{\Lambda}\Sigma$ and its charge-conjugate partner[30,31]. The result was that only 0.57 % of the $\overline{\Lambda}\Lambda$ events with $\chi^2 < 5$ have also been accepted as $\overline{\Lambda}\Sigma^o$ events in a $\overline{\Lambda}\Sigma^o$ analysis. The ambiguous events have been excluded from the main data sample.

4 Results

4.1 Cross sections

In Fig. 8 the differential cross sections at 1.546 GeV/c and 1.695 GeV/c are shown as a function of the $\overline{\Lambda}$ centre-of-mass angle $\theta_{\overline{\Lambda}}$. Both angular distributions are anisotropic: they show a steep rise at forward angles and a relatively flat shape elsewhere. The angular distributions were fitted using a Legendre polynomial expansion,

$$\frac{d\sigma}{d\Omega}(\cos\theta_{\overline{\Lambda}}) = \sum_{k=0}^{k_{max}} a_k P_k(\cos\theta_{\overline{\Lambda}}) \ . \tag{2}$$

The resulting coefficients and reduced χ^2-values are given in Table 1. The best fits were obtained with coefficients up to third order at 1.546 GeV/c and up to sixth order at 1.695 GeV/c. This indicates contributions from d-waves at the lower beam momentum and even from f-waves at the higher one. Figure 9

displays the relative coefficients a_i/a_0 for the angular distributions at 1.546 and 1.695 GeV/c together with those obtained previously at 1.437, 1.445, 1.477, and 1.508 GeV/c [5,24]. Even close to threshold non–zero values of a_1/a_0 and a_2/a_0 indicate contributions from $l > 0$ partial waves.

In Fig. 10 the angular distributions are shown in a logarithmic scale as a function of the reduced four–momentum transfer squared, $t' = t - t(\cos\theta_{\overline{\Lambda}} = 1)$, where

$$t = m_{\rm p}^2 + m_\Lambda^2 - \tfrac{1}{2}s + \tfrac{1}{2}\left[(s - 4\,m_{\rm p}^2)(s - 4\,m_\Lambda^2)\right]^{1/2}\cos\theta_{\overline{\Lambda}} \ , \qquad (3)$$

$$t' = -\tfrac{1}{2}\left[(s - 4\,m_{\rm p}^2)(s - 4\,m_\Lambda^2)\right]^{1/2}(1 - \cos\theta_{\overline{\Lambda}}) \ . \qquad (4)$$

The steep rise approaches an exponential form for $t' > -0.2$ (GeV/c)^2 with similar slopes of (8.85 ± 0.30) and (8.67 ± 0.19) (GeV/c)$^{-2}$ at 1.546 and 1.695 GeV/c, respectively. This behaviour seems to be energy independent, since the previously measured differential cross sections for $\overline{\rm p}{\rm p} \to \overline{\Lambda}\Lambda$ at lower energies [5,24] show a similar average slope [32] of about $b \approx 8.5$ (GeV/c)$^{-2}$ for $t' > -0.15$ (GeV/c)^2.

The values of the integrated cross sections are $(44.6 \pm 0.9 \pm 3.3)\,\mu$b at 1.546 GeV/$c$ and $(70.0 \pm 1.1 \pm 5.1)\,\mu$b at 1.695 GeV/$c$ beam momentum, where the first error is statistical and the second systematic. A compilation of all integrated cross sections of the reaction $\overline{\rm p}{\rm p} \to \overline{\Lambda}\Lambda$ below 2.5 GeV/c is shown in Fig. 11 (ref. [5,24,33–36]).

4.2   Polarization

Owing to the parity–violating interference between s– and p–waves, the non–leptonic weak decays $\Lambda \to {\rm p}\pi^-$ and $\overline{\Lambda} \to \overline{\rm p}\pi^+$ are asymmetric. Since the p($\overline{\rm p}$) is preferentially emitted in (opposite to) the $\Lambda(\overline{\Lambda})$ spin direction, the polarizations and spin correlations can be determined by measuring the angular distributions of the decay baryons in the $\Lambda(\overline{\Lambda})$ rest frame. The coordinate system used for evaluation is shown in Fig. 12. Parity conservation in the hadronic process $\overline{\rm p}{\rm p} \to \overline{\Lambda}\Lambda$ restricts the Λ and $\overline{\Lambda}$ polarization to be nonzero only transverse to the production plane (i.e. the y–axis in Fig. 12, which is not to be confused with the vertical direction of the detector). The normalized angular distribution of the decay nucleons from $\Lambda \to {\rm p}\pi^-$ for a hyperon sample with polarization P is

$$I(\theta_y) = \frac{1}{4\pi}\left(1 + \alpha P \cos\theta_y\right) \ , \qquad (5)$$

where the angle θ_y is measured between the normal to the reaction plane (y–axis) and the nucleon direction in the Λ rest frame. The value of the decay asymmetry parameter α for $\Lambda \to {\rm p}\pi^-$ is known from other experiments [26] as $\alpha = 0.642 \pm 0.013$, and the corresponding parameter for $\overline{\Lambda} \to \overline{\rm p}\pi^+$ is given by $\overline{\alpha} = -\alpha$ [37]), if CP invariance is assumed.

The product αP and its standard deviation $\sigma(\alpha P)$ have been obtained from the data adapting the method of weighted sums [38]),

$$\alpha P = \frac{\sum_{i=1}^N \cos\theta_y^{(i)}}{\sum_{i=1}^N \cos^2\theta_y^{(i)}} \qquad \text{and} \qquad \sigma(\alpha P) = \left[\frac{1}{\sum_{i=1}^N \cos^2\theta_y^{(i)}}\right]^{1/2} \ , \qquad (6)$$

10

which only requires that the detector acceptance ϵ fulfills the symmetry condition $\epsilon(\theta_y) = \epsilon(180° - \theta_y)$. This symmetry condition is satisfied in the PS185 detector and thus no corrections are needed at the present level of statistical accuracy.

The polarizations of the Λ and $\overline{\Lambda}$ are obtained by dividing the products αP_Λ and $\overline{\alpha} P_{\overline{\Lambda}}$ by α and $\overline{\alpha}$, respectively. The resulting polarizations of the Λ and $\overline{\Lambda}$ hyperons at 1.546 and 1.695 GeV/c are given in Table 2 and are shown in Fig. 13 as a function of $\cos\theta_{\overline{\Lambda}}$. The quoted errors are statistical only. The sytematic errors arising from an error in the determination of the angles θ_y and from a wrong assignment of the baryon–number are negligible compared with the statistical errors. The background events produced on carbon show, with lower statistical accuracy, a polarization similar to the actual data (see Fig. 6). The systematic error of the polarization due to the events from $\overline{p}C \rightarrow \overline{\Lambda}\Lambda + X$ is therefore negligible.

The charge–conjugation invariance of the reaction $\overline{p}p \rightarrow \overline{\Lambda}\Lambda$ requires equal polarization of the hyperons and antihyperons for a given bin of $\cos\theta_{\overline{\Lambda}}$. Since this is fulfilled within the errors (see Fig. 13), the polarization values for Λ and $\overline{\Lambda}$ have been averaged and included in Fig. 13 and Table 2. At both momenta the averaged hyperon polarization is positive at forward angles and negative elsewhere. For 1.695 GeV/c the positive polarization at forward angles is weak.

The polarization data, measured at various incident momenta by the PS185 experiment, are displayed in Fig. 14 as a function of the four–momentum transfer squared t in an (s,t)–diagram, where s is the invariant mass squared. The data are embedded in a curve that represents the kinematical boundaries in the (s,t) plane. The right end of the horizontal bar at each invariant mass squared corresponds to the reduced four–momentum transfer squared $t' = 0\,(\text{GeV}/c)^2$. A notable fact is that the change of sign of the polarization occurs at $t' \approx -0.2\,(\text{GeV}/c)^2$ at all energies. This is the same value as that for which the turnover from a flat distribution to a forward rise appears in the differential cross sections $d\sigma/dt'$ (Fig. 10).

4.3   Spin Correlation

Considering the decays $\Lambda \rightarrow p\pi^-$ and $\overline{\Lambda} \rightarrow \overline{p}\pi^+$ simultaneously, the normalized spatial distribution of the decay protons and decay antiprotons in the Λ and $\overline{\Lambda}$ rest frames, respectively, has — for a given bin of $\cos\theta_{\overline{\Lambda}}$ — the form

$$I(\overline{\theta_i}, \theta_j) = \frac{1}{16\pi^2}\left[1 + \alpha P_\Lambda \cos\theta_y + \overline{\alpha} P_{\overline{\Lambda}} \cos\overline{\theta}_y + \alpha\overline{\alpha} \sum_{i,j} C_{ij} \cos\overline{\theta}_i \cos\theta_j\right] \quad (7)$$

with $i = \overline{x}, \overline{y}, \overline{z}$ and $j = x, y, z$. The angles $\theta_x, \theta_y, \theta_z$ $(\overline{\theta_x}, \overline{\theta_y}, \overline{\theta_z})$ are measured between the decay–proton (decay–antiproton) direction and the directions x, y, z $(\overline{x}, \overline{y}, \overline{z})$ in the Λ ($\overline{\Lambda}$) rest frame (see Fig. 12). The spin correlation coefficients C_{ij} are defined as normalized averages of products of the three Λ and three $\overline{\Lambda}$ spin components and they are evaluated according to[33]):

$$C_{ij} = \frac{9}{\alpha\overline{\alpha}}\frac{1}{N}\sum_{k=1}^{N}\left[\cos\overline{\theta}_i \cos\theta_j\right]_{(k)} \quad (8)$$

11

The standard deviations of these coefficients are

$$\sigma(C_{ij}) = \frac{1}{|\alpha\overline{\alpha}|} \left[\frac{9 - (\alpha\overline{\alpha}\,C_{ij})^2}{N}\right]^{1/2} \approx \frac{3}{|\alpha\overline{\alpha}|}\frac{1}{N^{1/2}} \;. \tag{9}$$

The nine coefficients are not all independent: charge–conjugation invariance requires $C_{ij} = C_{ji}$, and, owing to parity conservation, $C_{\overline{x}y} = C_{\overline{y}x} = C_{\overline{y}z} = C_{\overline{z}y} = 0$. Therefore only $C_{\overline{x}x}$, $C_{\overline{y}y}$, $C_{\overline{z}z}$ and $C_{\overline{x}z}=C_{\overline{z}x}$ may have non–zero values, and the spin correlation matrix becomes

$$\begin{pmatrix} C_{\overline{x}x} & C_{\overline{x}y} & C_{\overline{x}z} \\ C_{\overline{y}x} & C_{\overline{y}y} & C_{\overline{y}z} \\ C_{\overline{z}x} & C_{\overline{z}y} & C_{\overline{z}z} \end{pmatrix} \Longrightarrow \begin{pmatrix} C_{\overline{x}x} & 0 & C_{\overline{x}z} \\ 0 & C_{\overline{y}y} & 0 \\ C_{\overline{z}x} & 0 & C_{\overline{z}z} \end{pmatrix} \;. \tag{10}$$

The evaluation of the spin correlation coefficients is not as simple as in the case of the polarization. Whilst there is a maximum angle in the laboratory for decay baryons (e.g. 33.5° at 1.695 GeV/c), the decay pions can be emitted at all angles. Since the acceptance of our detector is limited at large angles, the acceptance for decay pions is not constant, in particular, pion tracks nearly parallel to the wire planes cannot be reconstructed. These losses in the laboratory system, when transformed into the $\Lambda(\overline{\Lambda})$ rest frame, may result in systematic errors of the spin correlation coefficients. Therefore an evaluation method was developed, which allowed those losses to be compensated using the charge–conjugation symmetry of the reaction $\overline{p}p \to \overline{\Lambda}\Lambda$ [39]). The evaluation method was tested by calculating the coefficients, which are required to be zero from parity conservation. All values obtained for those coefficients are compatible with zero.

The results of the spin correlation coefficients for the two incident momenta are given in Table 3. Since the coefficients $C_{\overline{x}z}$ and $C_{\overline{z}x}$ agree within the errors as required from charge–conjugation invariance, only the average values of $C_{\overline{x}z}$ and $C_{\overline{z}x}$ are presented. In Fig.15 the spin correlation coefficients are shown together at both momenta as a function of t'. There is a stringent agreement of these coefficients at both momenta. This indicates that the spin correlation coefficients as a function of t' are energy independent in this energy range.

From the spin correlation coefficients $C_{\overline{x}x}$, $C_{\overline{y}y}$ and $C_{\overline{z}z}$ the singlet fraction F_S, which is the expectation value of the spin singlet projection operator, can be calculated according to

$$F_S = \tfrac{1}{4}\left(1 - \langle\vec{\sigma}_{\overline{\Lambda}}\cdot\vec{\sigma}_\Lambda\rangle\right) = \tfrac{1}{4}\left(1 + C_{\overline{x}x} - C_{\overline{y}y} + C_{\overline{z}z}\right) \;. \tag{11}$$

This has the values

$$F_S = \begin{cases} 0 & \text{for a pure triplet state,} \\ 1 & \text{for a pure singlet state,} \\ \tfrac{1}{4} & \text{for uncorrelated spin directions of the } \overline{\Lambda} \text{ and } \Lambda \;. \end{cases}$$

The values of F_S, which are displayed as a function of t' in Fig.16, are consistent with zero at both incident momenta. The average values of F_S are

$$\langle F_S\rangle = -0.078 \pm 0.052 \quad \text{at } 1.546 \text{ GeV}/c$$
$$\text{and} \quad \langle F_S\rangle = -0.032 \pm 0.030 \quad \text{at } 1.695 \text{ GeV}/c \;.$$

12

This indicates that the $\overline{\Lambda}\Lambda$ pairs are produced in a pure triplet state.

The background events produced on carbon show, with smaller statistical accuracy, a singlet fraction F_S similar to the actual data (see Fig. 6). The systematic error of F_S due to the events from $\overline{p}C \rightarrow \overline{\Lambda}\Lambda + X$ is therefore negligible. However, the slightly negative values of F_S indicate the order of magnitude of remaining systematic errors of the evaluation method.

4.4 CP Invariance

The reaction $\overline{p}p \rightarrow \overline{\Lambda}\Lambda$ offers the opportunity of looking for a violation of the CP invariance in the $\overline{\Lambda}\Lambda$ system by comparing the asymmetry parameters α and $\overline{\alpha}$. Because of the simultaneous and exclusive production of the $\overline{\Lambda}\Lambda$ pairs, systematic errors are reduced. A violation of CP invariance would be indicated by a non–zero ratio

$$A = \frac{\alpha + \overline{\alpha}}{\alpha - \overline{\alpha}} \quad . \tag{12}$$

The charge–conjugation invariance of the hadronic $\overline{\Lambda}\Lambda$ production requires for the hyperon polarizations $P_\Lambda = P_{\overline{\Lambda}}$. Therefore A can be determined from the measured quantities αP_Λ and $\overline{\alpha} P_{\overline{\Lambda}}$ by

$$A = \frac{\alpha P_\Lambda + \overline{\alpha} P_{\overline{\Lambda}}}{\alpha P_\Lambda - \overline{\alpha} P_{\overline{\Lambda}}} \tag{13}$$

without the necessity of knowing the absolute values of P_Λ , $P_{\overline{\Lambda}}$, α, and $\overline{\alpha}$.

Donoghue et al.[40,41] have obtained numerical estimates for the ratio A. The results vary for the different model assumptions, but typical values for the decay $\Lambda \rightarrow p\pi^-$ ($\overline{\Lambda} \rightarrow \overline{p}\pi^+$) are around 10^{-4}.

We have evaluated the ratio A for 10 (20) bins of $\cos\theta_{\overline{\Lambda}}$ at $1.546\,\mathrm{GeV}/c$ ($1.695\,\mathrm{GeV}/c$) in order to study a possible angular dependence of A and to exclude bins with polarization values, which are too small for a reasonable calculation of A according to Eq. 13. The mean value $\langle A \rangle$ is obtained by averaging over the angular distribution. The influence of the finite bin size on $\langle A \rangle$ has been studied using different bin widths. It was found that the values of $\langle A \rangle$ do not change significantly. The results are

$$\langle A \rangle = -0.07 \pm 0.09 \quad \text{at } 1.546 \text{ GeV}/c^{\,25)} \quad ,$$
$$\langle A \rangle = 0.006 \pm 0.073 \quad \text{at } 1.695 \text{ GeV}/c \quad ,$$

which gives a weighted average value for both incident momenta of

$$\langle A \rangle = -0.024 \pm 0.057 \quad .$$

The quoted errors are statistical ones, all other errors are negligible in comparison with the statistical errors. The method for the determination of the ratio A is described in more detail in ref.[25]. The value for A reported in this paper is more precise than all others previously obtained[25,42,43]. It should be noted, however, that a measurement of A to a precision of 10^{-4} would require of the order of 10^9 reconstructed events[44].

13

5 Conclusion

In this paper results from a study of the reaction $\bar{p}p \to \bar{\Lambda}\Lambda$ at two incident momenta, 1.546 GeV/c and 1.695 GeV/c, are presented. They correspond to excess energies above threshold ($\epsilon = \sqrt{s} - 2m_\Lambda$) of $\epsilon = 39.1$ MeV and $\epsilon = 91.7$ MeV, respectively.

The differential cross sections are anisotropic at both energies, showing a steep rise at forward angles and a relatively flat shape elsewhere. Fits of the angular distributions using a Legendre polynomial expansion indicate contributions up to d–waves at the lower energy and up to f–waves at the higher one. Our earlier work demonstrated that p–waves and perhaps even higher l–values contribute all the way down to threshold. The differential cross sections show a typical behaviour as a function of the reduced four–momentum transfer squared t'. At both energies the shapes of the differential cross sections approach an exponential form $a \cdot \exp(bt')$ for $t' > -0.2$ (GeV/c)^2 with similar slopes of $b = 8.85 \pm 0.30$ and $b = 8.67 \pm 0.19$ (GeV/c)$^{-2}$ at 1.546 and 1.695 GeV/c, respectively. This behaviour seems to be approximately energy independent in this energy range, since previously measured differential cross sections for $\bar{p}p \to \bar{\Lambda}\Lambda$ at lower energies show a similar average slope of about $b \approx 8.5$ (GeV/c)$^{-2}$ for $t' > -0.15$ (GeV/c)^2.

Owing to the 'self–analysing' properties of the weak Λ and $\bar{\Lambda}$ decays, the polarization and spin correlation of the hyperons can be measured without the necessity for a secondary scattering. The polarizations of the Λ and $\bar{\Lambda}$ agree within the errors as required from the charge–conjugation invariance of the hadronic process $\bar{p}p \to \bar{\Lambda}\Lambda$. The hyperon polarization is positive at forward angles and strongly negative elsewhere. A notable fact is that the change of sign of the polarization, viewed as a function of the reduced four–momentum transfer squared, occurs at $t' \approx -0.2$ (GeV/c)^2 for all energies between threshold and the ones presented in this paper. This is also about the same value of t' as that for which the turnover shows up from a flat distribution to a forward rise in the differential cross sections $d\sigma/dt'$.

The high statistics in comparison with previous measurements allowed for the first time a meaningful extraction of the spin correlation coefficients at single excess energies. The coefficients at the two energies as a function of the reduced four–momentum transfer squared show a striking agreement, which indicates that the spin correlation coefficients are energy independent in this energy range.

At both energies the singlet fractions F_S, derived from the spin correlation coefficients, are compatible with zero, indicating that the $\bar{\Lambda}\Lambda$ are produced in a pure triplet state.

The simultaneous measurement of the Λ and $\bar{\Lambda}$ offers the possibility of evaluating the ratio $A = (\alpha + \bar{\alpha})/(\alpha - \bar{\alpha})$ of the asymmetry parameters α and $\bar{\alpha}$ of the weak $\Lambda \to p\pi^-$ and $\bar{\Lambda} \to \bar{p}\pi^+$ decays, which is required to be zero from CP invariance. The weighted average value for both incident momenta is $\langle A \rangle = -0.024 \pm 0.057$, which is the most precise result obtained so far from hyperon non–leptonic decays.

14

References

1) A.Bialas and K. Zalewski, Nucl. Phys. **B6** (1968) 449

2) H.J.Lipkin, Phys. Rep. **8** (1973) 173

3) J.C.Kluyver et al., Nucl. Phys. **B140** (1978) 141

4) B.E. Bonner et al., Phys. Rev. Lett. **58** (1987) 447

5) P.D. Barnes et al., Phys. Lett. **B229** (1989) 432

6) H.W. Atherton, B.R. French, J.P. Moebes and E. Quercigh,
Nucl. Phys. **B69**(1974) 1

7) P.F. Loverre et al., Z. Phys. **C6** (1980) 283;
M. Abramovich et al., Nucl. Phys. **B27** (1971) 477

8) R. Haas, T. Miczaika, U. Opara, K. Quabach and W.J. Schwille,
Nucl. Phys. **B137** (1978) 261

9) G. Bunce et al., Phys. Rev. Lett. **36** (1976) 1113

10) H. Genz and S. Tatur, Phys. Rev. **D30** (1984) 63

11) F. Tabakin and R.A. Eisenstein, Phys. Rev. **C31** (1985) 1857

12) H.R. Rubinstein and H. Snellman, Phys. Lett. **165** (1985) 187

13) M. Kohno and W. Weise, Phys. Lett. **B179** (1986) 15,
Phys. Lett. **B206** (1988) 584, Nucl. Phys. **A479** (1988) 433

14) J.A. Niskanen, Helsinki University preprint HU-TFT-86-28 (1986)

15) S. Furui and A. Faessler, Nucl. Phys. **A468** (1987) 669

16) M. Burkardt and M. Dillig, Phys. Rev. **C37** (1988) 1362

17) R.G.E. Timmermans, T.A. Rijken and J.J. de Swart, Nucl. Phys. **A479**
(1988) 383

18) M.A. Alberg, E.M. Henley, L. Wilets and P.D. Kunz,
Nucl. Phys. **A508** (1990) 323c;
M.A. Alberg, K. Bräuer, E.M. Henley and L. Wilets, Proc. IVth LEAR
Workshop, Villars-sur-Ollon, 1987, eds. C. Amsler et al. (Harwood, Chur,
1988) 361

19) O.D. Dalkarov, K.V. Protasov and I.S. Shapiro,
Int. J. Mod. Phys. **A5** (1990) 2155;
O.D. Dalkarov and K.V. Protasov, Proc. IVth LEAR Workshop, Villars-
sur-Ollon, 1987, eds. C. Amsler et al. (Harwood, Chur, 1988) 365

20) Th. Hippchen, B. Holzenkamp, K. Holinde and J. Speth, Proc. IVth LEAR
Workshop, Villars-sur-Ollon, 1987, eds. C. Amsler et al. (Harwood, Chur,
1988) 371

21) P. Lafrance, B. Loiseau and R. Vinh Mau, Proc. IVth LEAR Workshop,
Villars-sur-Ollon, 1987, eds. C. Amsler et al. (Harwood, Chur, 1988) 375;
P. Lafrance and B.Loiseau,
University of Paris preprint IPNO/TH 90-32 (1990)

22) I.S. Shapiro, Proc. IVth LEAR Workshop, Villars-sur-Ollon, 1987, eds.
C. Amsler et al. (Harwood, Chur, 1988) 377

23) W. Roberts, Harvard University preprint HUTP-90/A020 (1990)

24) P.D. Barnes et al., Phys. Lett. **B189** (1987) 249

25) P.D. Barnes et al., Phys. Lett. **B199** (1987) 147

26) Particle Data Group, Review of Particle Properties,
Phys. Letters **B204**(1988) 230

27) A. Breskin, G. Charpak, B. Gabioud, F. Sauli, N. Trautner, W. Duinker
and G. Schulz, Nucl. Instr. and Meth. **119** (1974) 9

28) W. Dutty, J. Franz, N. Hamann, R. Peschina, E. Rössle, H.Schledermann,
H. Schmitt and H.G. Ulmer, Nucl. Instr. and Meth. **A252** (1986) 570

29) W. Dutty, Dissertation, University of Freiburg (1988)

30) P.D. Barnes et al., Phys. Lett. **B246** (1990) 273

31) S. Ohlsson, Dissertation (number 249), Uppsala University (1990)

32) H. Schmitt et al., Proc. IXth European Symposium on Proton-Antiproton
Interactions and Fundamental Symmetries, Mainz, 1988, eds. K. Kleinknecht
and E. Klempt, Nucl. Phys. B (Proc. Suppl.) 8 (1989) 173

33) B. Jayet et al., Nuovo Cimento **45A** (1978) 371;
B. Jayet, Thesis No. 263, Ecole Polytechnique Lausanne (1976)

34) B.Y. Oh, P.S. Eastman, Z. Ming Ma, D.L. Parker, G.A. Smith and
R.J. Sprafka, Nucl. Phys. **B51** (1973) 57

35) J. Badier, A. Bonnet, Ph. Briandet and B. Sadoulet,
Phys. Lett. **B25** (1967) 152

36) N. Kwak, J.E. Manweiler and M.L. Nicholas,
Nuovo Cimento **23A** (1974) 610

37) A. Pais, Phys. Rev. Lett. **3** (1959) 242

38) D. Besset, B. Favier, L.G. Greeniaus, R. Hess, C. Lechanoine,
D. Rapin and D.W. Werren, Nucl. Instr. and Meth. **166** (1979) 515

39) G. Sehl, Dissertation, JÜL.-SPEZ-535, Jülich (1989)

40) J.F. Donoghue, X.G. He and S. Pakvasa, Phys. Rev. **D34** (1986) 833

41) J.F. Donoghue, Proc. 3rd Conf. on the Intersections between Particle and
Nuclear Physics, Rockport (Maine), 1988, ed. G.M. Bunce (AIP Conference
Proceedings No. 176, American Institute of Physics, New York, 1988), 341

42) P. Chauvat et al., Phys. Lett. **B163** (1985) 273

43) M.H. Tixier et al., Phys. Lett. **B212** (1988) 523

44) N. Hamann, preprint CERN-EP/89-69 (1989)

Table 1: Results for the Legendre polynomial fits (Eq. 2) of the differential cross sections of $\bar{p}p \to \bar{\Lambda}\Lambda$ at 1.546 and 1.695 GeV/c for several maximum orders k_{max}.

1.546 GeV/c incident momentum				
k_{max}	1	2	3	4
χ^2_{red}	25.530	7.210	1.204	1.246
a_0	2.768 ± 0.066	3.379 ± 0.074	3.531 ± 0.075	3.537 ± 0.075
a_1/a_0	0.704 ± 0.046	0.948 ± 0.043	1.087 ± 0.045	1.091 ± 0.045
a_2/a_0		0.903 ± 0.049	1.101 ± 0.053	1.117 ± 0.057
a_3/a_0			0.562 ± 0.055	0.583 ± 0.063
a_4/a_0				0.048 ± 0.063

1.695 GeV/c incident momentum				
k_{max}	1	2	3	4
χ^2_{red}	31.1	15.6	5.93	0.864
a_0	3.474 ± 0.050	4.400 ± 0.062	5.073 ± 0.072	5.494 ± 0.078
a_1/a_0	0.659 ± 0.028	0.997 ± 0.029	1.256 ± 0.033	1.356 ± 0.033
a_2/a_0		0.799 ± 0.032	1.145 ± 0.037	1.403 ± 0.042
a_3/a_0			0.646 ± 0.034	0.942 ± 0.040
a_4/a_0				0.473 ± 0.035
k_{max}	5	6	7	8
χ^2_{red}	0.788	0.547	0.562	0.580
a_0	5.525 ± 0.079	5.565 ± 0.081	5.564 ± 0.081	5.563 ± 0.081
a_1/a_0	1.371 ± 0.035	1.380 ± 0.036	1.379 ± 0.036	1.379 ± 0.036
a_2/a_0	1.429 ± 0.046	1.465 ± 0.048	1.464 ± 0.049	1.463 ± 0.049
a_3/a_0	0.991 ± 0.049	1.049 ± 0.054	1.044 ± 0.056	1.043 ± 0.057
a_4/a_0	0.523 ± 0.045	0.618 ± 0.055	0.612 ± 0.060	0.609 ± 0.064
a_5/a_0	0.072 ± 0.038	0.164 ± 0.049	0.154 ± 0.061	0.151 ± 0.066
a_6/a_0		0.123 ± 0.041	0.114 ± 0.053	0.110 ± 0.067
a_7/a_0			−0.012 ± 0.045	−0.016 ± 0.058
a_8/a_0				−0.005 ± 0.048

Table 2: Polarization of $\overline{\Lambda}$ and Λ and average polarization for $\overline{\Lambda}$ and Λ as a function of $\cos\theta_{\overline{\Lambda}}$ and t' at 1.546 and 1.695 GeV/c incident momentum.

1.546 GeV/c incident momentum				
$\langle\cos\theta_{\overline{\Lambda}}\rangle$	$\langle t'\rangle$ [(GeV/c)^2]	$P_{\overline{\Lambda}}$	P_{Λ}	$P_{(\overline{\Lambda},\Lambda)}$
−0.90	−0.509	−0.053 ± 0.177	−0.297 ± 0.167	−0.182 ± 0.122
−0.70	−0.456	−0.385 ± 0.165	−0.536 ± 0.165	−0.461 ± 0.117
−0.50	−0.402	−0.412 ± 0.162	−0.484 ± 0.162	−0.448 ± 0.115
−0.30	−0.349	−0.419 ± 0.162	−0.475 ± 0.162	−0.447 ± 0.114
−0.10	−0.295	−0.702 ± 0.184	−0.588 ± 0.176	−0.642 ± 0.127
0.10	−0.241	−0.423 ± 0.163	−0.189 ± 0.163	−0.306 ± 0.116
0.30	−0.188	−0.396 ± 0.152	−0.046 ± 0.149	−0.217 ± 0.107
0.45	−0.147	−0.104 ± 0.153	0.201 ± 0.157	0.045 ± 0.110
0.55	−0.121	0.374 ± 0.152	0.582 ± 0.155	0.476 ± 0.109
0.65	−0.094	0.586 ± 0.135	−0.181 ± 0.143	0.225 ± 0.098
0.75	−0.067	0.353 ± 0.124	0.194 ± 0.121	0.272 ± 0.087
0.85	−0.040	0.355 ± 0.113	0.321 ± 0.116	0.338 ± 0.081
0.95	−0.013	0.308 ± 0.108	0.121 ± 0.107	0.214 ± 0.076

1.695 GeV/c incident momentum				
$\langle\cos\theta_{\overline{\Lambda}}\rangle$	$\langle t'\rangle$ [(GeV/c)^2]	$P_{\overline{\Lambda}}$	P_{Λ}	$P_{(\overline{\Lambda},\Lambda)}$
−0.90	−0.841	−0.013 ± 0.125	−0.244 ± 0.119	−0.134 ± 0.086
−0.70	−0.753	−0.245 ± 0.122	−0.391 ± 0.120	−0.320 ± 0.086
−0.50	−0.664	−0.508 ± 0.108	−0.489 ± 0.104	−0.498 ± 0.075
−0.30	−0.575	−0.228 ± 0.098	−0.395 ± 0.101	−0.309 ± 0.070
−0.10	−0.487	−0.567 ± 0.101	−0.375 ± 0.100	−0.470 ± 0.071
0.10	−0.398	−0.402 ± 0.098	−0.468 ± 0.098	−0.435 ± 0.069
0.30	−0.310	−0.306 ± 0.092	−0.331 ± 0.088	−0.319 ± 0.064
0.45	−0.243	−0.077 ± 0.119	−0.203 ± 0.115	−0.142 ± 0.082
0.55	−0.199	0.065 ± 0.097	0.047 ± 0.097	0.056 ± 0.068
0.65	−0.155	−0.022 ± 0.086	0.009 ± 0.085	−0.006 ± 0.060
0.75	−0.111	0.094 ± 0.074	−0.001 ± 0.075	0.048 ± 0.053
0.85	−0.066	0.173 ± 0.065	0.066 ± 0.064	0.119 ± 0.046
0.95	−0.022	0.074 ± 0.055	0.090 ± 0.056	0.082 ± 0.039

Table 3: Spin correlation coefficients C_{ij} and singlet fraction F_S
as a function of $\cos\theta_{\bar{\Lambda}}$ and t' at 1.546 and 1.695 GeV/c incident momentum.

			1.546 GeV/c incident momentum			
$\langle\cos\theta_{\bar{\Lambda}}\rangle$	$\langle t'\rangle$ [(GeV/c)^2]	$C_{\bar{x}x}$	$C_{\bar{y}y}$	$C_{\bar{z}z}$	$\langle C_{\bar{x}z}, C_{\bar{z}x}\rangle$	F_S
-0.80	-0.482	1.024 ± 0.353	0.361 ± 0.353	-0.020 ± 0.353	-0.017 ± 0.250	0.411 ± 0.153
-0.40	-0.375	0.390 ± 0.356	1.023 ± 0.356	-1.375 ± 0.356	0.455 ± 0.252	-0.252 ± 0.154
0.00	-0.268	0.775 ± 0.363	1.370 ± 0.363	-1.283 ± 0.363	-0.079 ± 0.256	-0.220 ± 0.157
0.40	-0.161	0.459 ± 0.268	1.104 ± 0.268	-1.131 ± 0.268	-0.509 ± 0.189	-0.194 ± 0.116
0.80	-0.054	-0.353 ± 0.176	0.710 ± 0.176	-0.233 ± 0.176	-0.354 ± 0.124	-0.074 ± 0.076

			1.695 GeV/c incident momentum			
$\langle\cos\theta_{\bar{\Lambda}}\rangle$	$\langle t'\rangle$ [(GeV/c)^2]	$C_{\bar{x}x}$	$C_{\bar{y}y}$	$C_{\bar{z}z}$	$\langle C_{\bar{x}z}, C_{\bar{z}x}\rangle$	F_S
-0.90	-0.841	-0.163 ± 0.339	-0.234 ± 0.339	-0.045 ± 0.339	-0.060 ± 0.240	0.256 ± 0.147
-0.70	-0.752	-0.806 ± 0.343	0.535 ± 0.343	-0.196 ± 0.343	-0.047 ± 0.242	-0.134 ± 0.148
-0.50	-0.664	-0.103 ± 0.310	-0.198 ± 0.310	-0.319 ± 0.310	0.201 ± 0.219	0.194 ± 0.134
-0.30	-0.575	-0.283 ± 0.292	-0.289 ± 0.292	-0.674 ± 0.292	-0.353 ± 0.207	0.083 ± 0.127
-0.10	-0.487	-0.298 ± 0.296	0.696 ± 0.296	-0.592 ± 0.296	0.360 ± 0.210	-0.147 ± 0.128
0.10	-0.398	0.761 ± 0.286	0.818 ± 0.286	-0.771 ± 0.286	0.329 ± 0.202	0.043 ± 0.124
0.30	-0.310	1.071 ± 0.255	1.260 ± 0.255	-1.165 ± 0.255	0.265 ± 0.180	-0.089 ± 0.110
0.50	-0.221	0.772 ± 0.214	0.889 ± 0.214	-1.331 ± 0.214	-0.421 ± 0.151	-0.112 ± 0.093
0.70	-0.133	0.274 ± 0.160	0.706 ± 0.160	-0.686 ± 0.160	-0.436 ± 0.113	-0.030 ± 0.069
0.90	-0.044	-0.394 ± 0.121	0.681 ± 0.121	-0.195 ± 0.121	0.015 ± 0.085	-0.068 ± 0.052
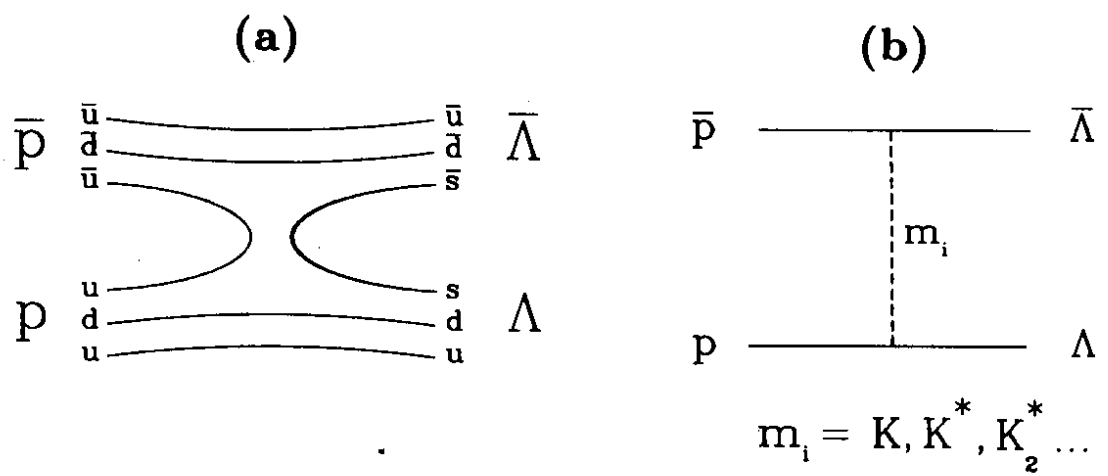
Figure 1: The reaction $\bar{p}p \to \bar{\Lambda}\Lambda$ viewed: a) as a $\bar{u}u$ quark–pair annihilation and $\bar{s}s$ creation process, b) as a t–channel meson exchange.
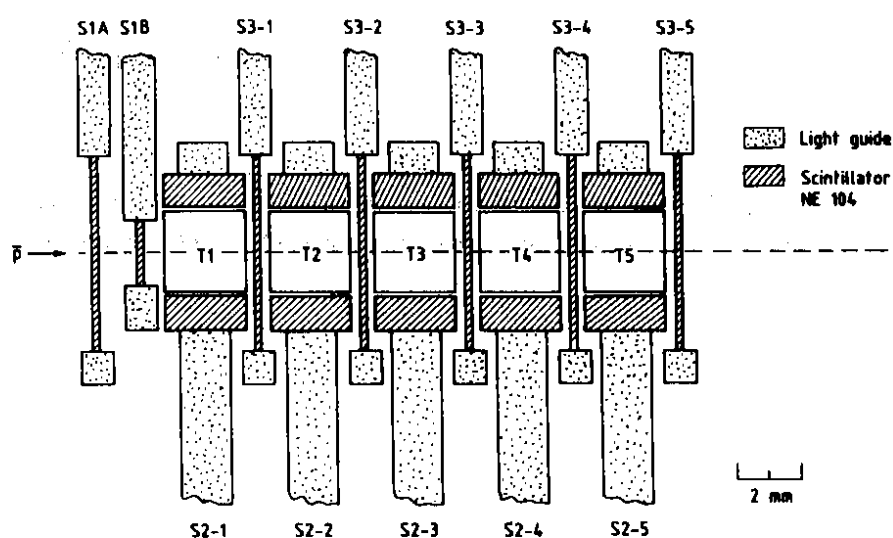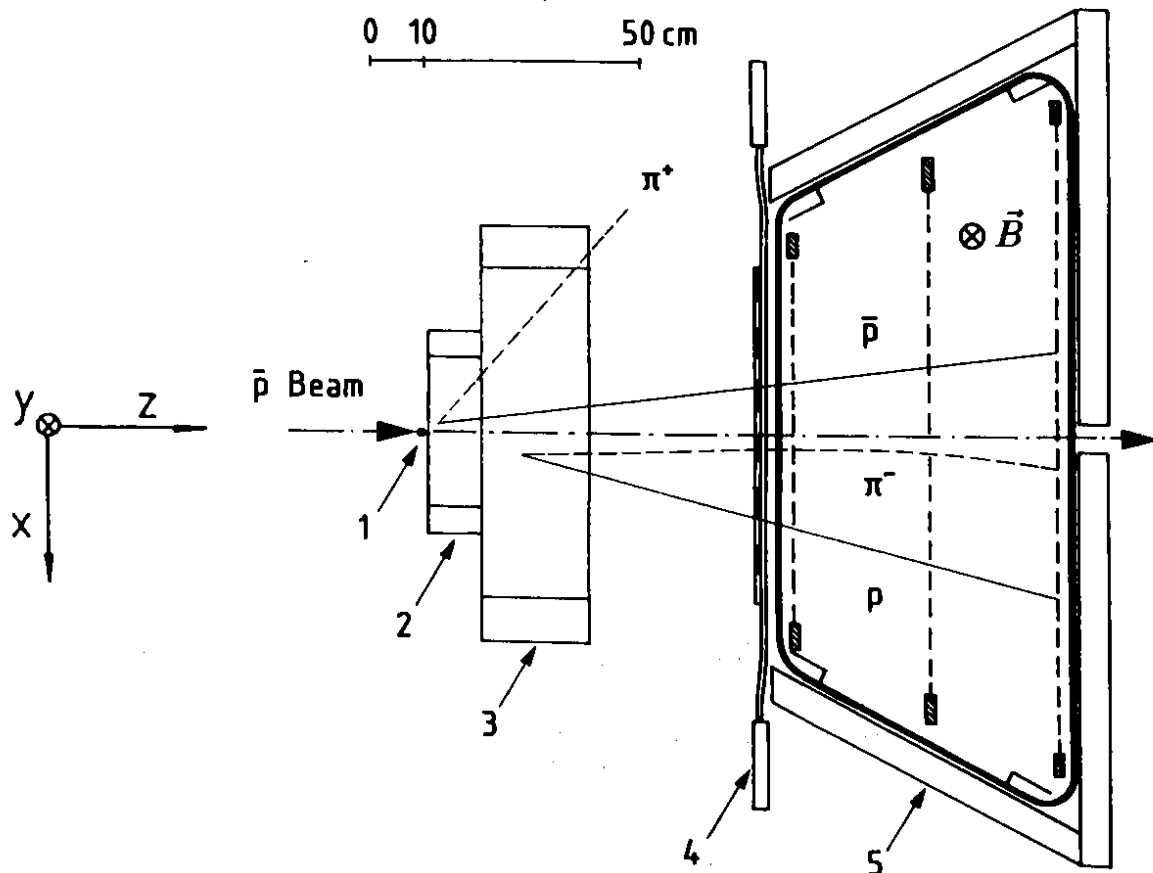
Figure 2: Set–up of experiment PS185 (upper part): **1** = active–trigger target, **2** = multiwire proportional chambers, **3** = drift chambers, **4** = scintillator hodoscope, and **5** = solenoid with drift chambers.

Scale drawing of the active–trigger target (lower part). The incoming antiproton is defined by a coincidence between S1A and S1B. The first target is pure carbon, while targets T2–T5 are polyethylene (CH₂). The veto and beam–tagging counters for each cell are labelled by S2 and S3.
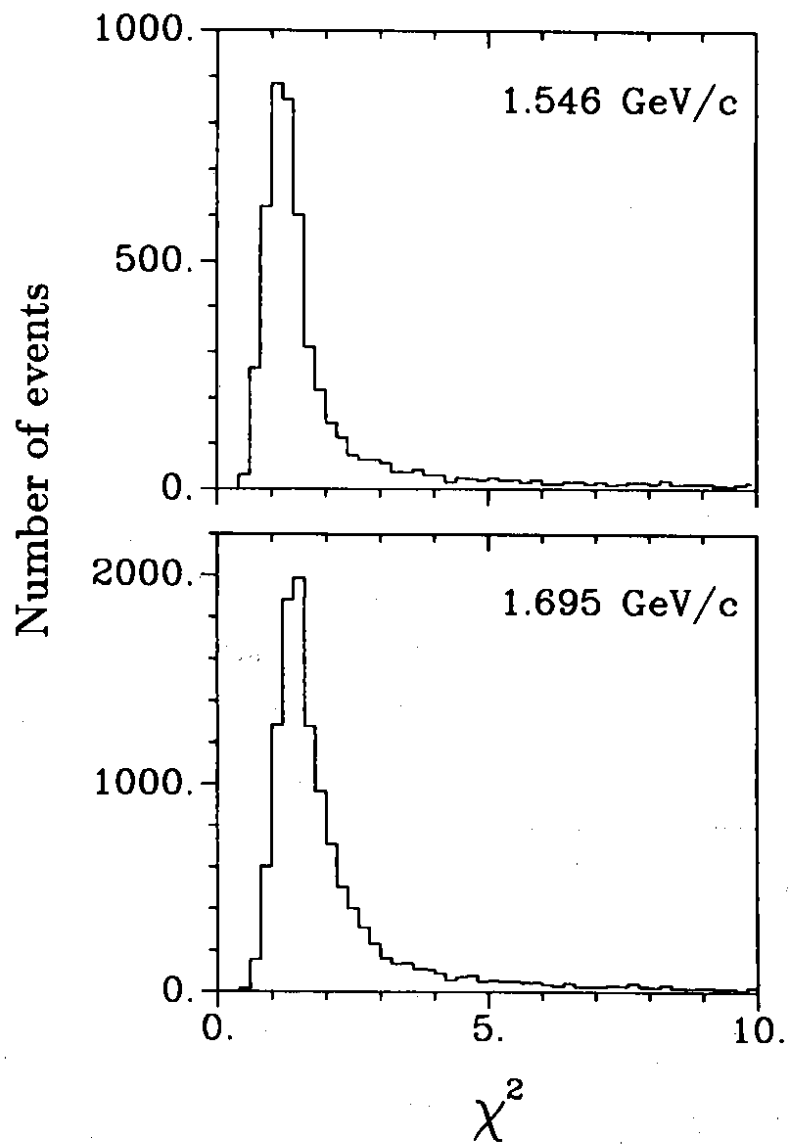
Figure 3: Reduced χ^2-distributions of the kinematical fits at 1.546 and 1.695 GeV/c.
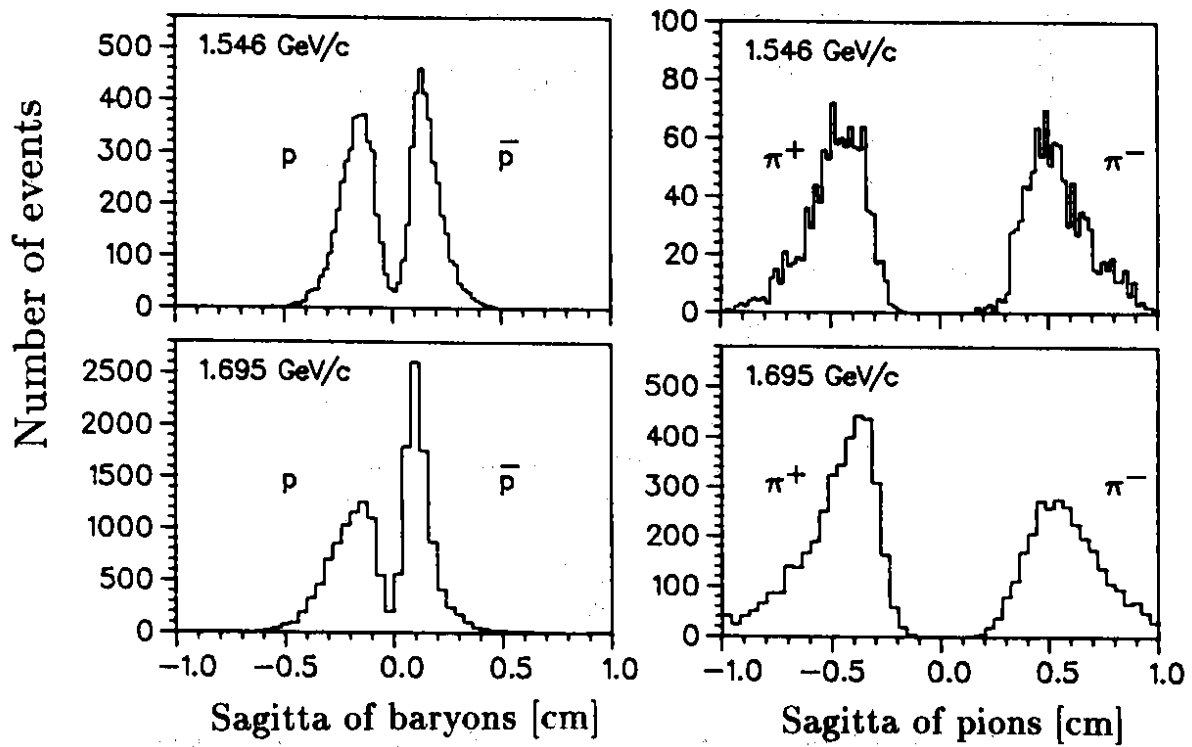
Figure 4: Sagitta distributions of decay particles from $\overline{\Lambda}\Lambda \rightarrow \overline{p}\pi^+p\pi^-$ for the magnetic field of 0.1 T at 1.546 and 1.695 GeV/c incident momentum.
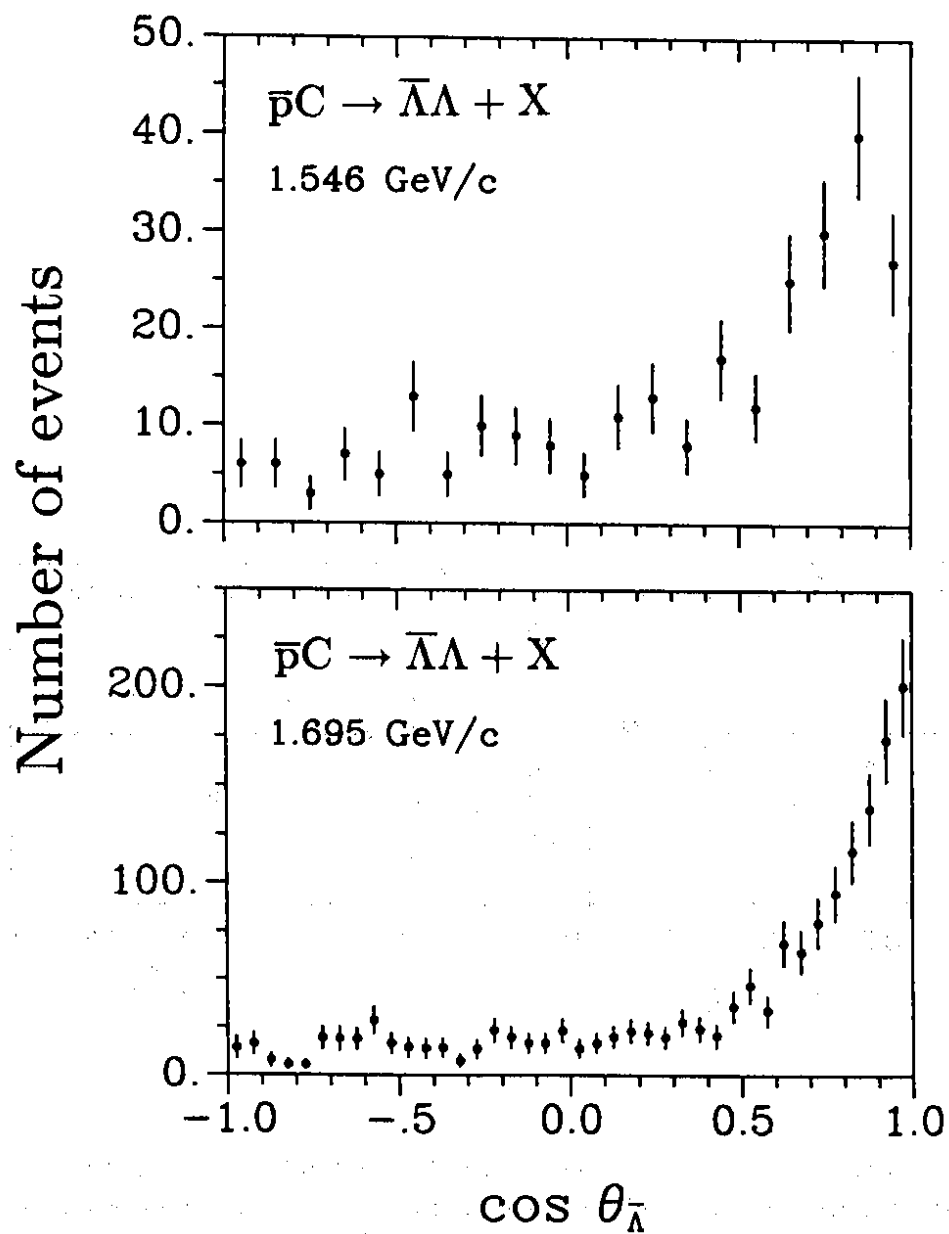
Figure 5: Angular distributions of $\overline{\Lambda}\Lambda$ events from the carbon target ('carbon background') at 1.546 and 1.695 GeV/c incident momentum as a function of the $\overline{\Lambda}$ centre–of–mass angle. The events have been analysed with cuts assuming the reaction $\overline{p}p \to \overline{\Lambda}\Lambda$.
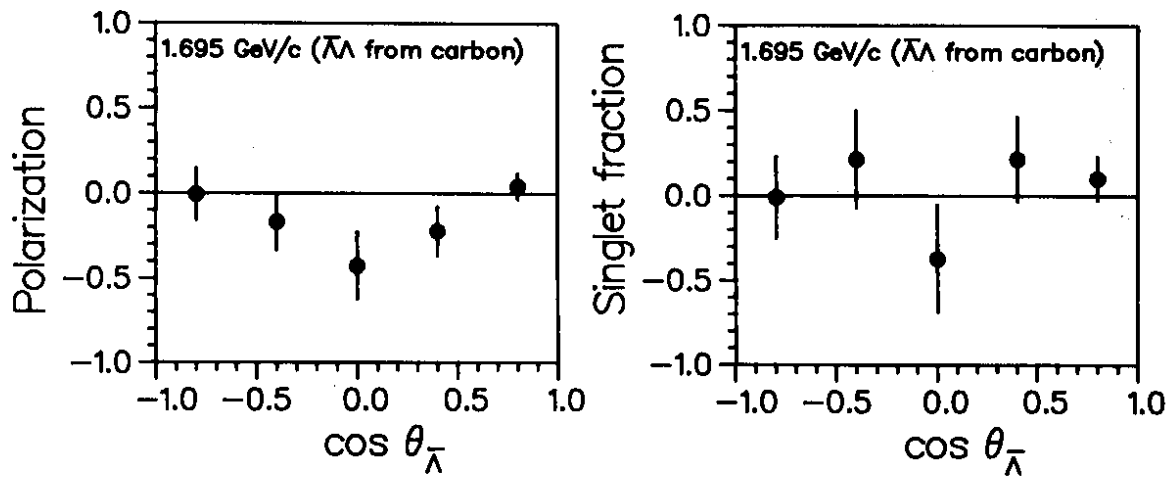
Figure 6: Polarization and singlet fraction for $\overline{\Lambda}\Lambda$ events from the carbon target ('carbon background') at 1.695 GeV/c incident momentum as a function of the $\overline{\Lambda}$ centre–of–mass angle. The events have been analysed with cuts assuming the reaction $\overline{p}p \rightarrow \overline{\Lambda}\Lambda$.
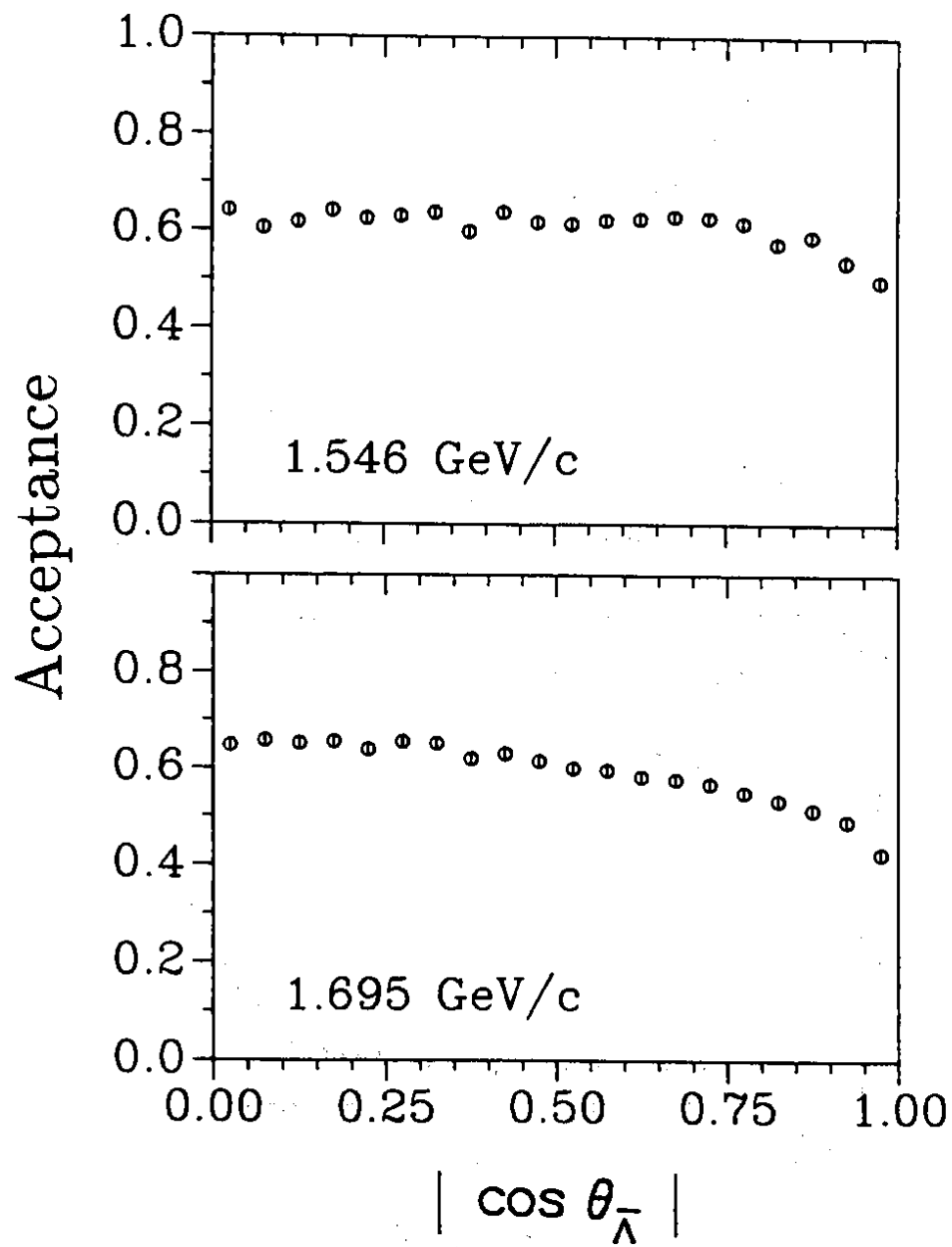
Figure 7: Detector acceptance for $\overline{\Lambda}\Lambda \to \bar{p}\pi^+p\pi^-$ events as a function of the $\overline{\Lambda}$ centre–of–mass angle, obtained from a Monte Carlo study of isotropically produced $\bar{p}p \to \overline{\Lambda}\Lambda$ events at 1.546 and 1.695 GeV/c.
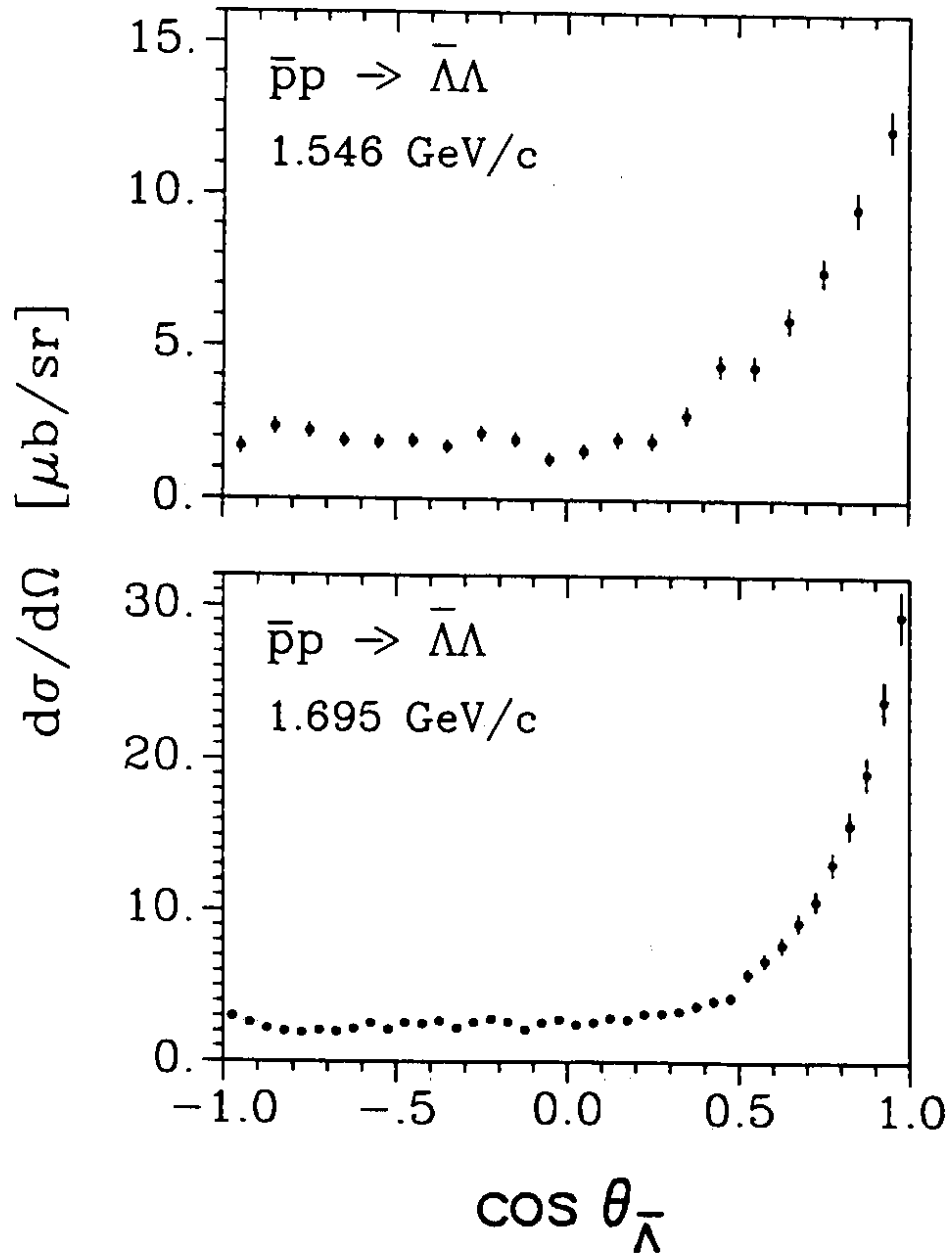
Figure 8: Differential cross sections at 1.546 and 1.695 GeV/c as a function of the $\bar{\Lambda}$ centre-of-mass angle.
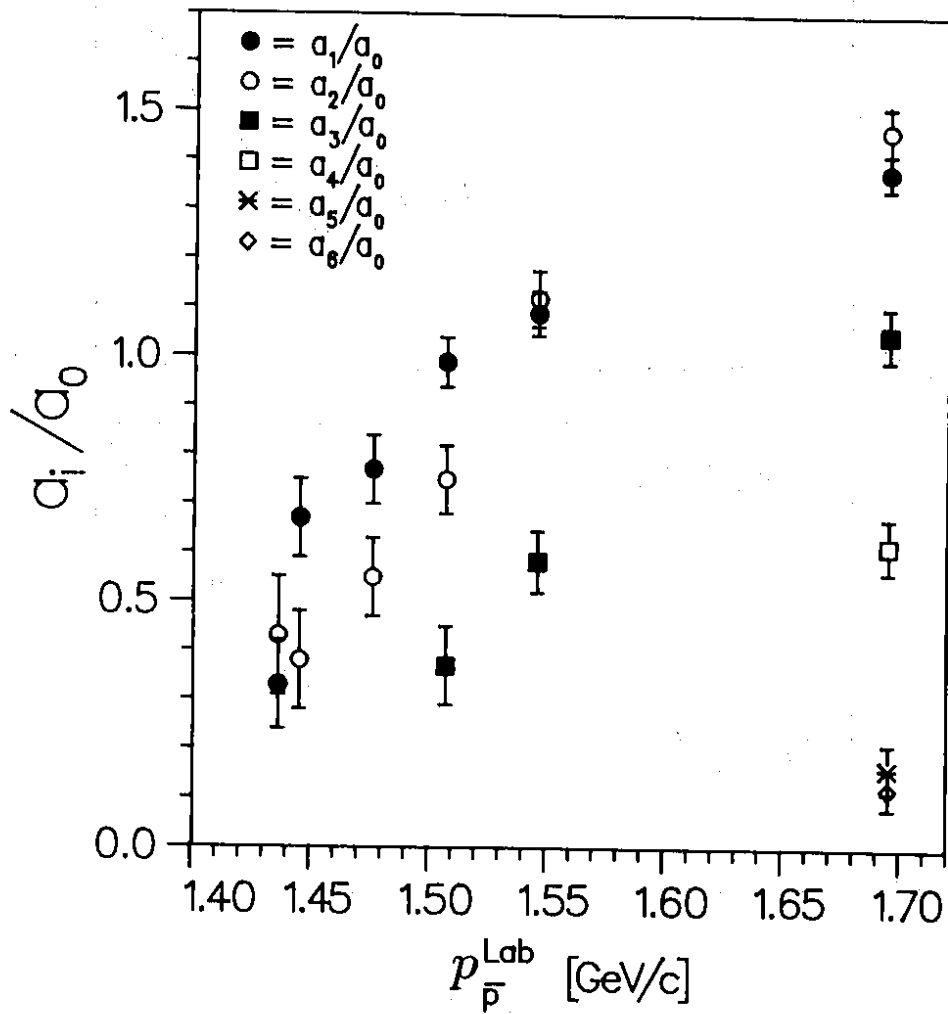
Figure 9: Relative Legendre coefficients as a function of the incident momentum. The data for the lower momenta are from Refs.[5,24]. The threshold for $\bar{\Lambda}\Lambda$ production is at 1.435 GeV/c.
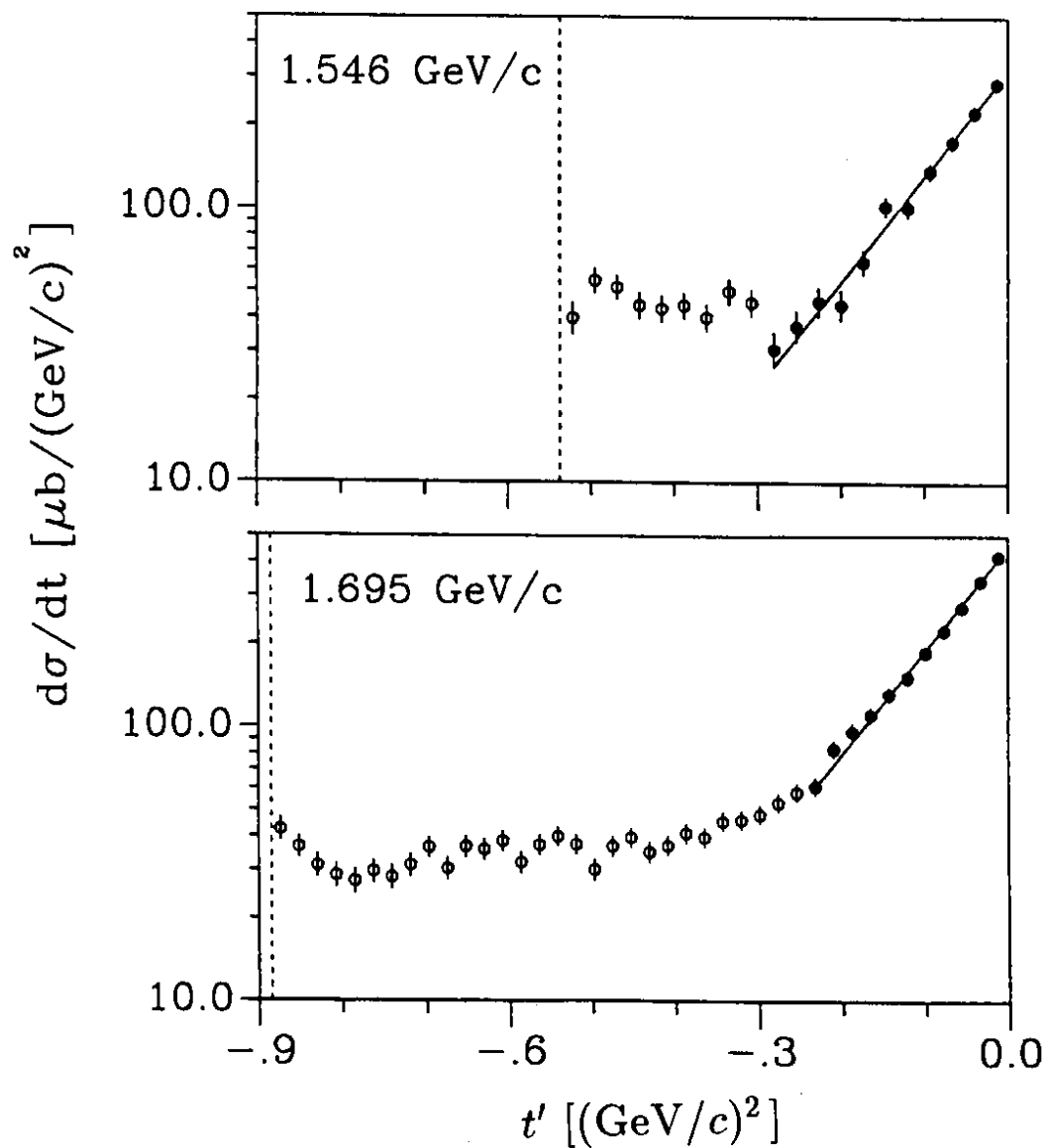
Figure 10: Differential cross sections at 1.546 GeV/c and 1.695 GeV/c as a function of t'. The lines are exponential fits of the form $a\exp(bt')$ with a slope of $b = 8.85 \pm 0.30\,(\mathrm{GeV}/c)^{-2}$ at $1.546\,\mathrm{GeV}/c$ and $b = 8.67 \pm 0.19\,(\mathrm{GeV}/c)^{-2}$ at $1.695\,\mathrm{GeV}/c$. The kinematically possible minimum values of t' at both momenta are indicated by dashed lines.
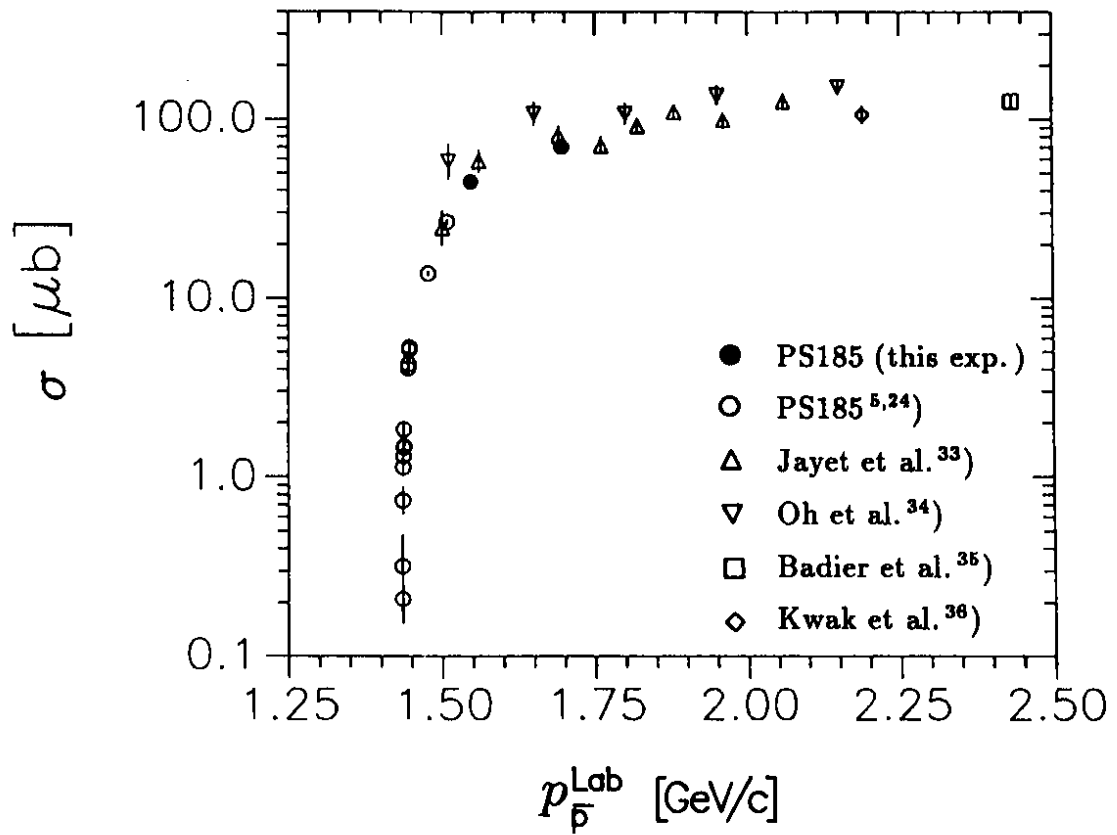
Figure 11: Integrated cross sections of the reaction $\bar{p}p \rightarrow \bar{\Lambda}\Lambda$ for incident momenta up to 2.5 GeV/c. The threshold for $\bar{\Lambda}\Lambda$ production is at 1.435 GeV/c.
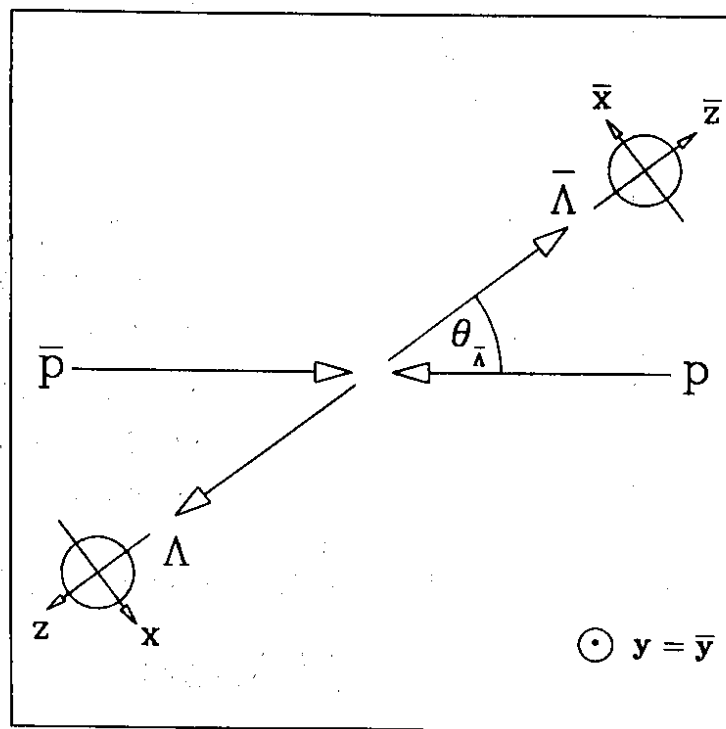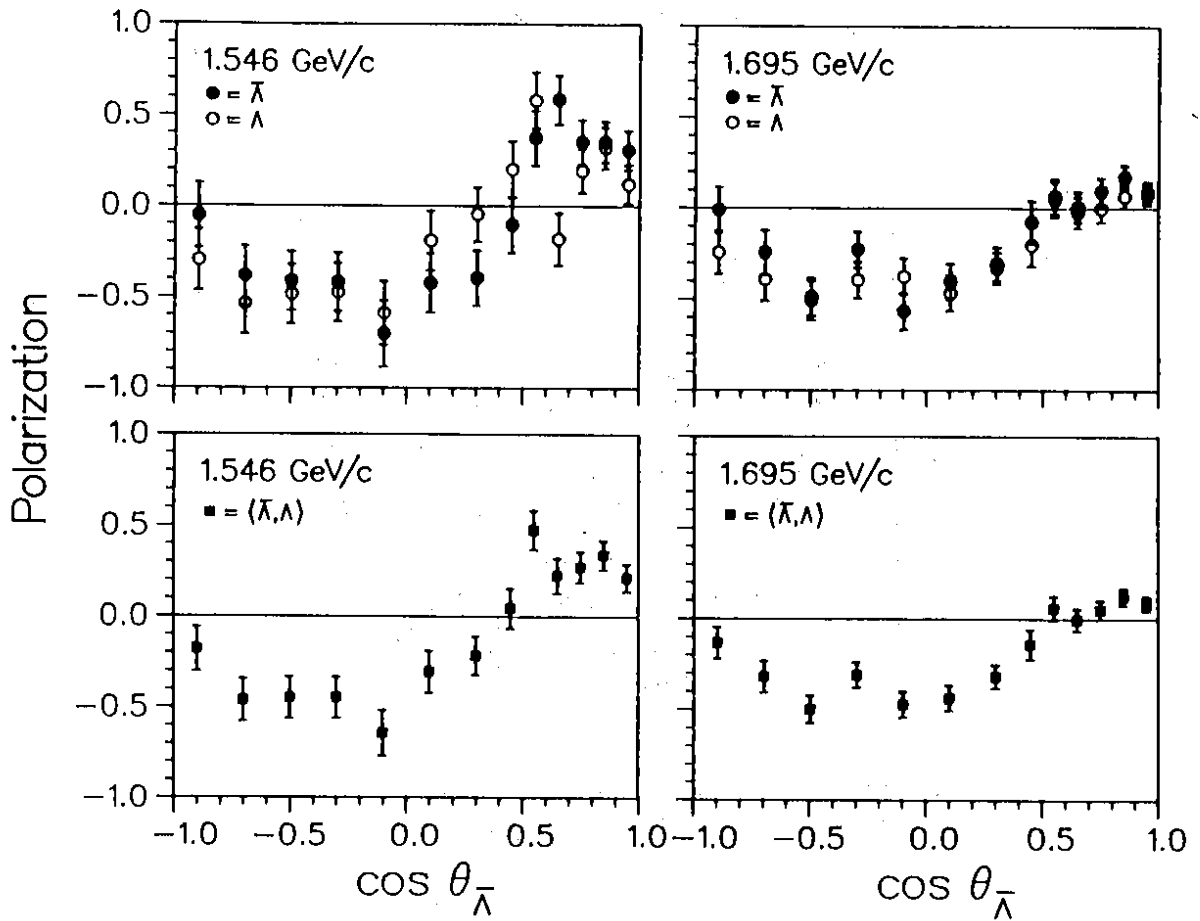
Figure 12: The coordinate system used in this paper

Figure 13: Polarization of $\overline{\Lambda}$ and Λ at 1.546 and 1.695 GeV/c as a function of the $\overline{\Lambda}$ centre–of–mass angle (upper part). Weighted mean of the $\overline{\Lambda}$ and Λ polarization at 1.546 and 1.695 GeV/c (lower part).
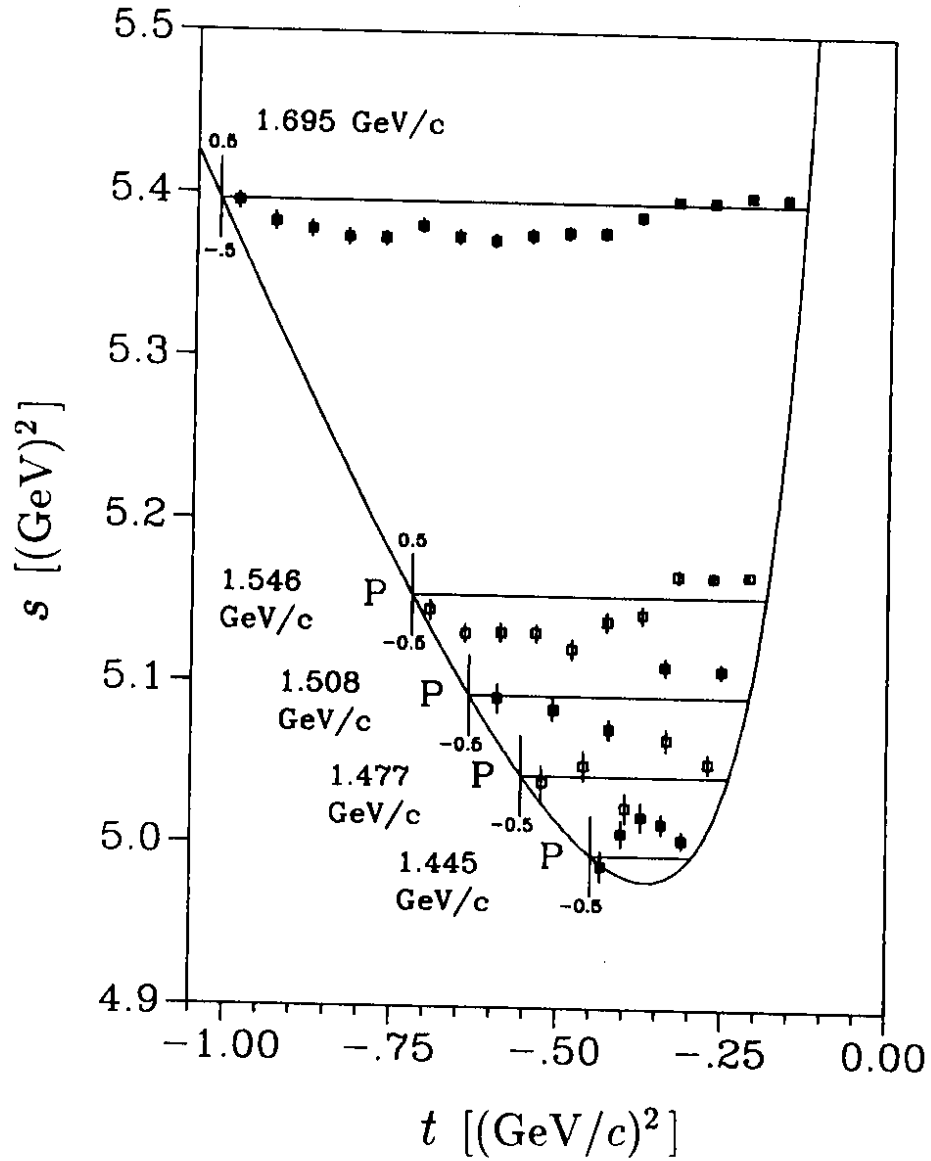
Figure 14: The polarization distributions measured by the PS185 Collaboration [5,24]) as a function of the four–momentum transfer squared t and the invariant mass squared s. The curve shows the kinematically allowed range of t for each value of s.
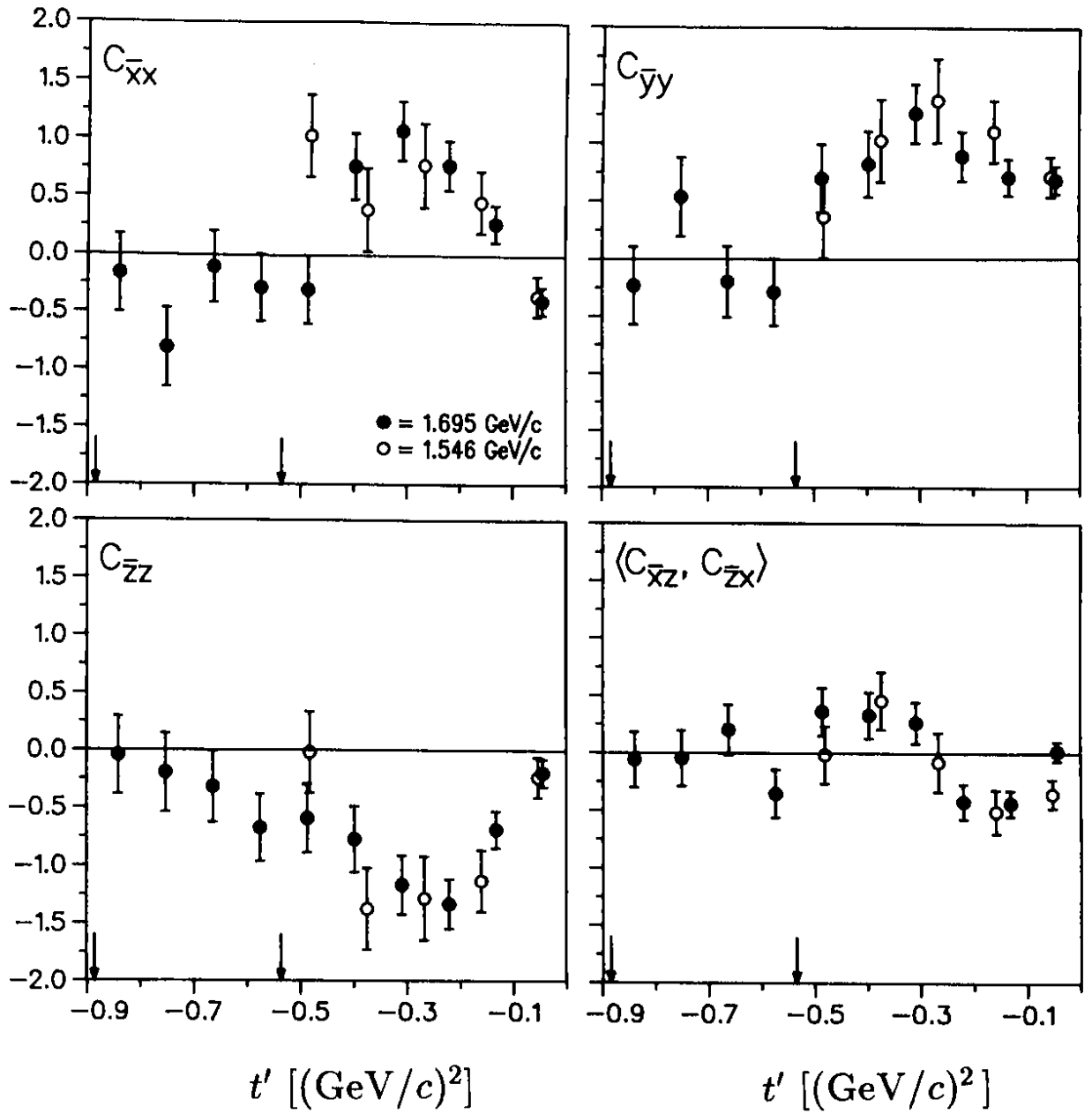
Figure 15: Spin correlation coefficients $C_{\bar{x}x}$, $C_{\bar{y}y}$, $C_{\bar{z}z}$ and mean value of $C_{\bar{x}z}$ and $C_{\bar{z}x}$ as a function of t' at 1.546 and 1.695 GeV/c. The kinematically possible minimum values of t' at both momenta are indicated by arrows.
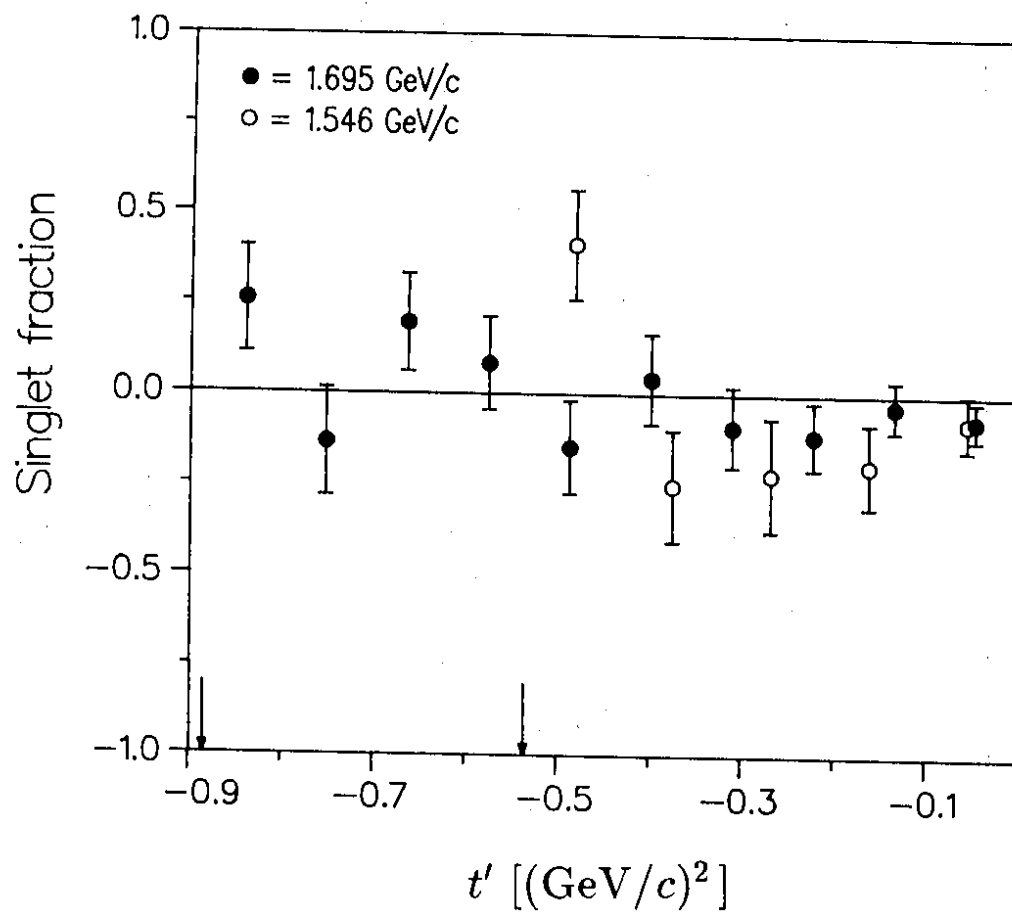
Figure 16: The singlet fraction F_S derived from the spin correlation coefficients as a function of t' at 1.546 and 1.695 GeV/c. The kinematically possible minimum values of t' at both momenta are indicated by arrows.